Nanoscale

Monodisperse Nanoparticles for Catalysis and Nanomedicine

Journal:	*Nanoscale*
Manuscript ID	NR-REV-07-2019-006080.R1
Article Type:	Review Article
Date Submitted by the Author:	01-Aug-2019
Complete List of Authors:	Muzzio, Michelle; Brown University, Department of Chemistry Li, Junrui; Brown University, Chemistry Yin, zhouyang; Brown University, Chemistry Delahunty, Ian; University of Georgia, Chemistry Xie, Jin; University of Georgia, Chemistry Sun, Shouheng; Brown University, Chemistry

Nanoscale

REVIEW

Monodisperse Nanoparticles for Catalysis and Nanomedicine

Michelle Muzzio,[a] Junrui Li,[a] Zhouyang Yin,[a] Ian Michael Delahunty,[b] Jin Xie,[b] and Shouheng Sun*[a]

Received 00th January 20xx,
Accepted 00th January 20xx

DOI: 10.1039/x0xx00000x

The growth and breadth of nanoparticle (NP) research now encompasses many scientific and technologic fields, which has driven the want to control NP dimensions, structures and properties. Recent advances in NP synthesis, especially in solution phase synthesis, and characterization have made it possible to tune NP sizes and shapes to optimize NP properties for various applications. In this review, we summarize the general concepts of using solution phase chemistry to control NP nucleation and growth for the formation of monodisperse NPs with polyhedral, cubic, octahedral, rod, or wire shapes and complex multicomponent heterostructures. Using some representative examples, we demonstrate how to use these monodisperse NPs to tune and optimize NP catalysis of some important energy conversion reactions, such as the oxygen reduction reaction, electrochemical carbon dioxide reduction, and cascade dehydrogenation/hydrogenation for the formation of functional organic compounds in greener chemistry reaction conditions. Monodisperse NPs with controlled surface chemistry, morphologies and magnetic properties also show great potential for use in biomedicine. We highlight how monodisperse iron oxide NPs are made biocompatible and target-specific for biomedical imaging, sensing and therapeutic applications. We intend to provide readers some concrete evidence that monodisperse NPs have been established to serve as successful model systems for understanding structure-property relationships at the nanoscale and further to show great potentials for advanced nanotechnological applications.

Introduction

Nanoparticles (NPs), commonly referred to as particles with dimensions less than 100 nm, are prevalent in nearly every facet of our lives. From potential applications in sustainable energy and therapeutics, to practical uses in art, agriculture, chemical industries and every in-between, the widespread embrace of "nano-" has been met by exciting research and even more research challenges. These drive the need to control the synthesis of NPs in order to realize the desired functionalities that are essential for applications.[1] Interestingly, the applications of NPs have been around for hundreds of years, without detailed understanding of what the nanoscale even was. For example, nanostructured Cu, Ag and Au were used to colour ceramics and glass 500 – 1,000 years ago.[2] Only within the last twenty years, however, has the technology been available for careful design of NPs, and with this, the desire to control the NPs with precise dimensions and enhanced properties has taken flight.

In the endeavour to make better NPs, monodispersity has risen as a measure of quality control. For NPs to be defined as monodisperse, their standard deviation in diameter (or in one dimension) should be less than ten percent.[3] Monodisperse NPs are the ideal model systems for understanding property tuning and optimization at the nanoscale. While it is well-known that nanomaterials behave very differently than bulk materials,[4] fine tuning of NP properties can only be possible when the NPs are

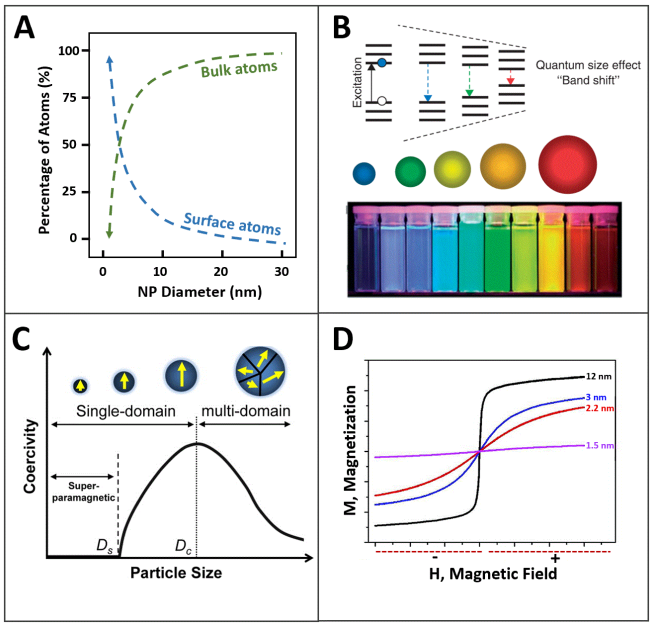

Fig. 1: (A) The relationship between NP size and the percentage of atoms on the surface or within the bulk of the NP, **(B)** Band gap tuning through NP size control in QDs (Adapted from ref. 7b with permission, Copyright 2010 John Wiley & Sons, Inc.), **(C)** Coercivity dependence on NP size in magnetic NPs (Adapted from ref. 8a with permission, Copyright 1996 American Chemical Society), and **(D)** the effect of NP size on magnetization, using iron oxide NPs as a model (Adapted from ref. 8b with permission, Copyright 2011 American Chemical Society).

[a] *Department of Chemistry, Brown University, Providence, Rhode Island 02912 USA. Email: ssun@brown.edu*
[b] *Department of Chemistry, University of Georgia, Athens, Georgia 30602 USA.*

monodisperse and structure-property relationships can be understood.

As the size of NPs decrease, the percentage of surface atoms exponentially increase, as summarized in **Fig. 1A**. Chemically, this increase in surface atoms provides more binding sites in the same molar amount of NPs, an important factor of any NP application, especially catalysis in which the surface of NPs allows for chemical reactions, complementing catalyst-support interactions.[5] Physically, the size of NPs is also critical to determine optoelectronics and magnetism.[1b,6] The size effects of monodisperse NPs on NP properties are evident in semiconducting NPs, also referred to as quantum dots (QDs), in their band gap/optics tuning (**Fig. 1B**), where larger QDs exhibit a narrower band gap, red-shifting the wavelength of absorption/emission light.[7] In magnetic NPs, size is also paramount in determining magnetic coercivity and magnetization.[8] NPs at a material-specific critical diameter (D_c) allow to support only a single magnetic domain within which magnetization reversal is decided by magnetocrystalline anisotropy energy, leading to the increase in magnetic coercivity, as illustrated in **Fig. 1C**. Magnetization direction of NPs smaller than D_c are subject to thermal agitation, and at a material-specific dimension D_s, they become superparamagnetic and show no coercivity. The increased number of surface atoms in smaller NPs further degrades the magnetization values (**Fig. 1D**) due to the presence of larger fraction of surface atoms that are often magnetically "silent" due to the surface oxidation/binding state. Therefore, a rigorous demand for monodisperse NP syntheses has come to meet the rising standards of NP functionality in every one of their widespread applications.

Recent advances in NP synthesis have reached the level that most NPs can now be made monodisperse, allowing deeper fundamental understanding of NP structure-property relationships for various applications, including those related to our daily life in energy, medicine and the environment. This review focuses on the general syntheses of monodisperse NPs as well as the application of these monodisperse NPs in catalysis and biomedicine, as outlined in **Fig. 2**.

The review first summarizes the general concept of making monodisperse NPs though both thermodynamic and kinetic growth conditions to achieve desired NP size and shape controls. It then highlights the applications of monodisperse NPs as catalysts for fuel cell reactions, the electrochemical reduction of carbon dioxide (CO_2) and greener chemical syntheses of value-added chemicals. It further highlights the applications of monodisperse NPs as probes for biomedical imaging, sensing and therapy. A great number of excellent publications on monodisperse NPs have been available, which makes any comprehensive review writing very challenging. In this review, we chose to use some examples published from our own group, plus a few representative examples from other publications to highlight the key ideas of the syntheses of monodisperse NPs and their applications in catalysis and biomedicine.

Synthesis of Monodisperse NPs

Monodisperse NPs are normally synthesized via solution phase reactions in which NP nucleation and growth can be better controlled, as illustrated in **Fig. 3**.[9] There are two main types of syntheses that can yield monodisperse NPs: *burst nucleation* and *seed-mediated growth*. In each synthetic process the general components typically needed are a solvent, monomers (or NP precursors), surfactant (also called capping agent/stabilizing agent/ligand) and reductant if the reduction of NP precursors is necessary.[10] The solvent is chosen as the reaction medium in which the NP precursor can react uniformly for NP formation, and the surfactant is present to react with the NP surface to form a layer of coating for NP stabilization during and after NP synthesis. There are many parameters that may be tuned to obtain stable monodisperse NPs. Therefore, care must be taken in the synthesis to ensure the reaction conditions are well-controlled to prepare NPs with certain sizes and shapes.

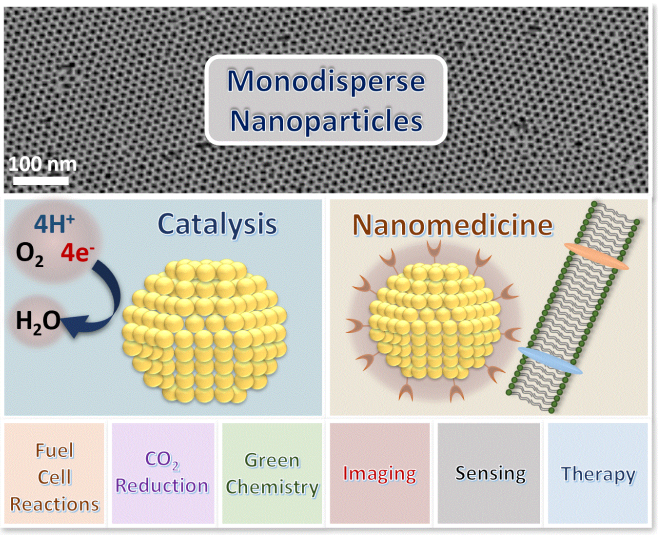

Fig. 2: Outline of the content of this review on monodisperse NPs and their applications in catalysis and nanomedicine.

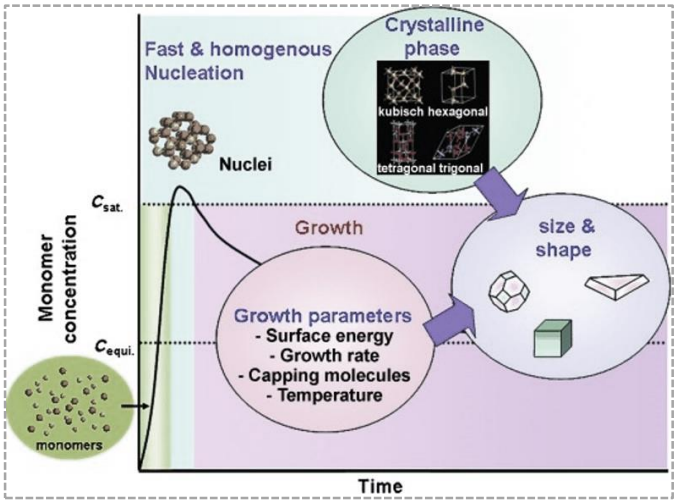

Fig. 3: General schematic of NP synthesis starting from the fast formation of nuclei and subsequent growth with common synthetic parameters that can be used to control NP sizes and shapes. Reprinted ref. 9a with permission, Copyright 2006 John Wiley & Sons, Inc.

To achieve burst nucleation, the growing monomers should be generated in a very short period of time to allow their concentration to reach the nucleation threshold, over which nuclei are formed.[11] Nucleation of NPs is not thermodynamically favoured and external energy is required to accomplish this process. Once nuclei are formed, monomers can be added to these nuclei, and the reaction enters the growth stage. This is a thermodynamically favoured process as the formation of the extra surface binding lowers the system free energy. This is also an important reason why a surfactant must be present in the reaction solution to slow down or even stop this spontaneous growth process to ensure the NPs at a certain size range can be stabilized in the reaction solution. In this process, many factors can affect the NP growth, including NP surface energy, growth rate, and the surfactant chemistry.[9,12] In a thermodynamic growth condition, stable polyhedral NPs are often obtained. For example, monodisperse Au NPs are synthesized in tetralin *via* reduction of $HAuCl_4$ in the presence of oleylamine **(Fig. 4A)**.[13] Magnetic Co NPs are synthesized via thermal decomposition of $Co(CO)_8$, in the presence of dioctylamine and oleic acid (**Fig. 4B**).[14] This metal carbonyl decomposition chemistry has also be used to prepare Fe NPs from the decomposition of $Fe(CO)_5$ in oleylamine solution of 1-octadecene (**Fig. 4C**).[15] When particle precursor chemistry is well-controlled, the solution phase synthesis can lead to large-scale preparation of Fe_3O_4 NPs with NP sizes tuneable in 1 nm increments as highlighted by 12 nm Fe_3O_4 NPs (**Fig. 4D**) synthesized through the thermal decomposition of a Fe-oleate complex.[16]

To prepare alloy NPs, the reaction leading to alloy component nucleation and growth must be even more carefully controlled. For example, in the preparation of alloy FePt NPs,

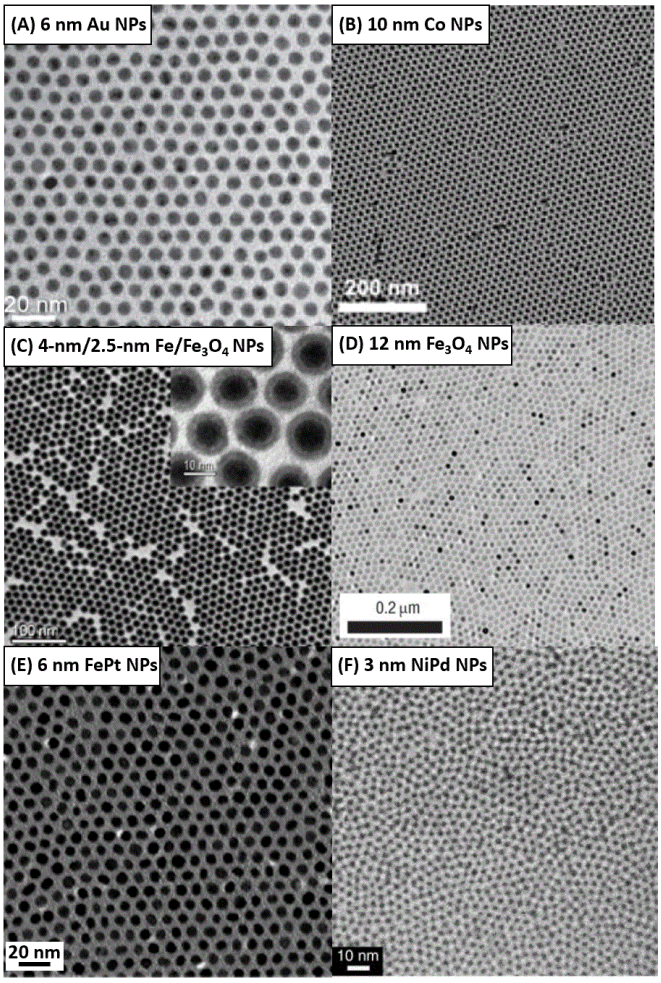

Fig. 4: TEM images of **(A)** 5 nm Au NPs (Reprinted from ref. 13b, Copyright 2008 Tsinghua Press and Springer-Verlag GmbH), **(B)** 10 nm Co NPs (Reprinted from ref. 8c with permission, Copyright 2015 American Chemical Society), **(C)** 4 nm Fe NPs with controlled Fe_3O_4 shell (Reprinted from ref. 15 with permission, Copyright 2006 American Chemical Society), **(D)** 12 nm Fe_3O_4 NPs synthesized through metal oleate decomposition (Reprinted from ref. 16 with permission, Copyright 2004 Springer Nature), **(E)** alloy FePt NPs (Reprinted from ref. 17b with permission, Copyright 2004 American Chemical Society), and **(F)** alloy NiPd NPs (Reprinted from ref. 18b with permission, Copyright 2018 John Wiley & Sons, Inc.).

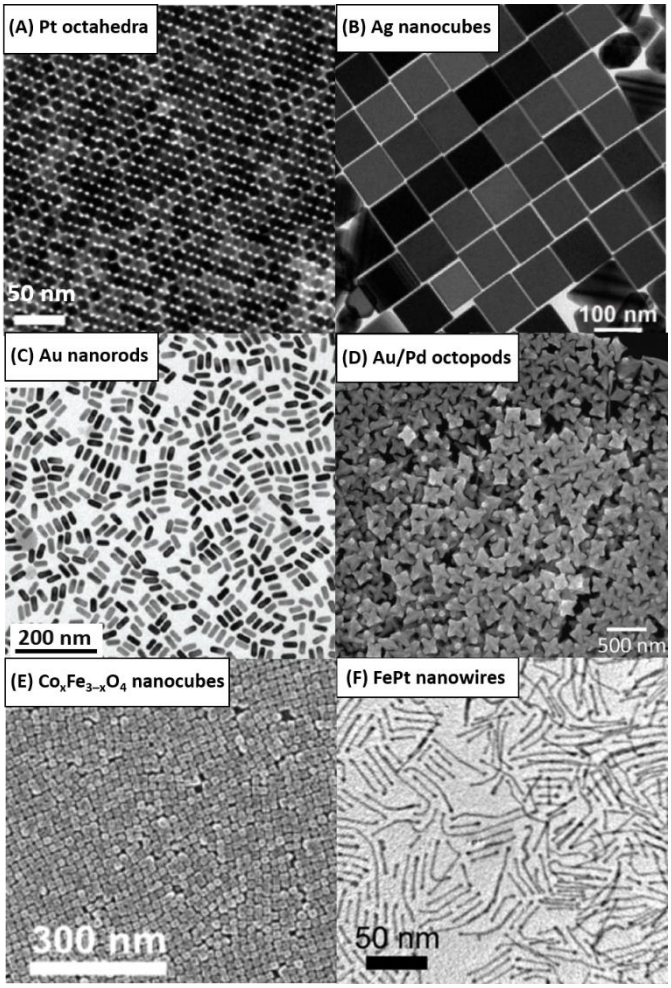

Fig. 5: (A) TEM image of an assembly formed from Pt octahedra (Reprinted from ref. 22b with permission, Copyright 2013 American Chemical Society), **(B)** TEM image of Ag nanocubes (Reprinted from ref. 23a with permission, Copyright 2016 American Chemical Society), **(C)** TEM image of Au nanorods (Reprinted from ref. 25 with permission, Copyright 2012 American Chemical Society), **(D)** scanning electron microscopy (SEM) image of Au/Pd octopods (Reprinted from ref. 26 with permission, Copyright 2011 American Chemical Society), **(E)** SEM of an assembly of $Co_xFe_{3-x}O_4$ nanocubes (Reprinted from ref. 27 with permission, Copyright 2014 American Chemical Society), and **(F)** TEM image of FePt nanowires (Reprinted from ref. 29b with permission, Copyright 2013 John Wiley & Sons, Inc.).

the Pt precursor, $Pt(acac)_2$, was reduced and $Fe(CO)_5$ decomposed at about 200 ˚C to initiate the nucleation of FePt alloy before the reaction temperature was raised further for FePt NP growth to occur and form 6 nm FePt NPs (**Fig. 4E**).[17] If two metal salt precursors are chosen for the formation of alloy NPs, the correct reducing agent should be used to reduce both metal salts concurrently, as demonstrated in the synthesis of 3 nm NiPd NPs (**Fig. 4F**) via co-reduction of $Pd(acac)_2$ and $Ni(OAc)_2$ by borane *tert*-butylamine at 100 ˚C in oleylamine solution of 1-octadecene.[18] This co-reduction method has been a popular choice for preparing various alloy NPs.[19]

When the growth of NPs is controlled at one specific crystal facet, edge or corner, different shaped NPs can be prepared. For example, polyhedral Pt NPs can be synthesized through the reduction of $Pt(acac)_2$ and stabilization by oleylamine and oleic acid in benzyl ether.[20] However, when metal carbonyl or pure CO is present, preferential exposure of Pt {100} facets are obtained during NP growth, giving Pt nanocubes.[21] Through control of CO amount, Pt octahedra (**Fig. 5A**), icosahedra, and hyper-branched uniform Pt structures could be synthesized.[22] Kinetic control over NP synthesis was better demonstrated in the synthesis of Ag and Pd nanocubes in the presence of Cl^- or Br^- ions.[23] Cl^- ions acted as a specific capping agent for the {100} facets, which allowed for the formation of sharp corners and edges of the nanocube, even at low temperatures (**Fig. 5B**). Kinetic control to prepare Au nanorods with uniform geometry and aspect ratios has been established through micelle-templated growth through the surfactant of hexadecyltrimethylammonium bromide (CTAB) and other reaction parameters like temperature and surfactant mixtures.[24] An additive, like salicylic acid, was proved imperative to increase the yield of Au nanorods (**Fig. 5C**) through modification of the micelle-formation of CTAB.[25] Controlling ratios of CTAB with ascorbic acid was also explored to control Au nanorod growth into more complicated NP structures, as demonstrated in the synthesis of core/shell Au/Pd octopods (**Fig. 5D**) and concave structures.[16] Reduction of $Fe(acac)_3$ and $Co(acac)_2$ in the presence of oleic acid and sodium oleate yielded monodisperse $Co_xFe_{3-x}O_4$ nanocubes (**Fig. 5E**).[17] Sodium oleate has been used in many NP syntheses to control the shape as well as aspect ratio of nanocubes, nanorods, and nanowires.[28] Comparable to the formation of Au nanorods, FePt nanorods/nanowires (**Fig. 5F**) were synthesized through tuning the ratio of oleylamine and 1-octadecene; more oleylamine resulted in longer nanowires.[29]

Seed-mediated growth differs from the conventional nucleation/growth process in that seeding NPs are pre-made and present in the reaction solution for further growth.[30] In this growth process, new nucleation processes should be avoided. The success of this synthesis is dependent primarily on the seed quality and the control of the growth on the seeding NP surface. Compared to the nucleation/growth approach, the seed-mediated growth method is advantageous to control not only NP sizes, but also NP structures and morphologies, such as

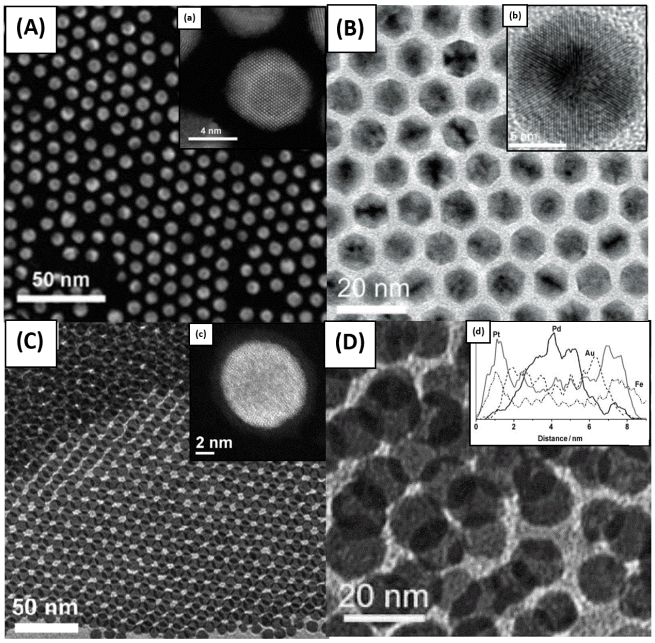

Fig. 6: (A) STEM image of Pd/Au core/shell NPs, high-resolution TEM shown in inset (Reprinted from ref. 31 with permission, Copyright 2010 John Wiley & Sons, Inc.), **(B)** TEM image of Au/Pd core/shell NPs high-resolution TEM shown in inset (Reprinted from ref. 32 with permission, Copyright 2012 John Wiley & Sons, Inc.), **(C)** TEM image of the assembly of Ni/FePt core/shell NPs, HAADF-STEM image of one NP shown in inset, (Reprinted from ref. 34 with permission, Copyright 2014 American Chemical Society), **(D)** TEM image of Pd/Au/FePt core/shell NPs, line-scan elemental analysis demonstrating the presence of two shells shown in inset (Reprinted from ref. 31 with permission, Copyright 2010 John Wiley & Sons, Inc.).

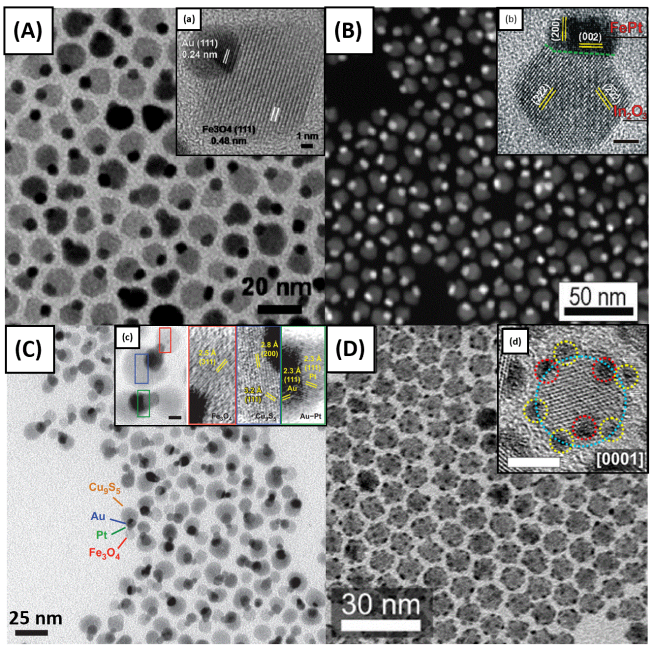

Fig. 7: (A) TEM image of Au-Fe_3O_4 dumbbell NPs, high-resolution TEM shown in inset (Reprinted from ref. 36 with permission, Copyright 2010 American Chemical Society), **(B)** STEM image of FePt-In_2O_3 dumbbell NPs, high resolution TEM shown in inset (Reprinted from ref. 40 with permission, Copyright 2011 American Chemical Society), **(C)** TEM image of Cu_xS-Au-Pt-Fe_3O_4 heterotetramer NPs, high resolution TEM of the individual components shown in inset, (Reprinted from ref. 42 with permission, Copyright 2011 Springer Nature), **(D)** TEM image of as-synthesized "patchy" Au-QD heterostructures, high-resolution TEM shown in inset (Reprinted from ref. 45 with permission, Copyright 2019 American Chemical Society).

core/shell NPs with controlled core dimension and shell thickness. In general, seeding monodisperse NPs are present, along with monomers for shell formation; a successful core/shell synthesis involves entering the growth stage on the seeding NP without individual nucleation of the shell materials. This strategy has been used to create both monodisperse Pd/Au (**Fig. 6A**)[31] and Au/Pd (**Fig. 6B**)[32] core/shell NPs, among many other bimetallic core/shell structures.[33] With proper synthetic control, a more complicated alloy shell can also be made, as demonstrated in the synthesis of Ni/FePt NPs (**Fig. 6C**).[34] Similarly, more shells can be grown in a core/shell structure through multiple growth steps, as seen in the synthesis of Pd/Au/FePt NPs (**Fig. 6D**).[31]

Seed-mediated growth method can be extended to prepare more complicated heterostructures to contain multiple components.[35] For example, bifunctional Au-Fe_3O_4 dumbbell NPs (**Fig. 7A**) could be synthesized through the controlled nucleation and growth of magnetic Fe_3O_4 on plasmonic Au NP seeds.[36] A similar approach was used to synthesize dual magnet FePt-Fe_3O_4,[37] and the post-modification could access more complex structures such as FePt-Fe_2C,[38] among others.[39] Semiconducting oxide, such as In_2O_3, can also be grown on the magnetic FePt NP surface (**Fig. 7B**).[40] *Via* similar seed-mediated growth, libraries of heterostructures have been discovered and studied.[41] **Fig. 7C** highlights successive heterostructure growth to form a chain of four different NP units.[42] To create this structure, Au was grown selectively on the Pt surface of the Pt-Fe_3O_4 dumbbell NPs. Further, Cu-S was added as the fourth component that preferentially grow on the Au surface. Such a strategy, combined with post-synthetic exchange mechanisms, has been used to create more combinations of complex heterostructures.[43] Recently, mechanisms about the crystallographic attachment as well as the assembly of heterostructures have also been explored.[44] In **Fig. 7D**, controlled growth of Au on CdSe-CdS QDs was made possible by the seed-mediated approach to create "patchy" heterostructures and further used to study controlled superlattice formation of heterostructures.[45]

Monodisperse NPs for Catalysis

General Catalytic Principles

The ever-increasing societal demands for energy consumption and industrial chemical production have triggered great efforts in seeking renewable and environmentally friendly energy/chemical conversion processes, such as fuel cells, batteries, and CO_2 or biomass conversion into valorized chemicals or fuels. The need to limit fossil fuel use and the fast-developing renewable energy and chemical industries require fundamental studies and efficient screenings of highly active and durable catalysts.[46] Recently, monodisperse NP catalysts for catalytic reactions for renewable energy/chemical production including oxygen reduction/oxidation reaction (ORR/OER),[47] hydrogen evolution/oxidation reaction (HER/HOR),[48] formic acid/alcohol oxidation reaction (FAOR/AOR),[49] CO_2 conversion and biomass conversion, have been extensively studied. Some emerging catalytic reactions, namely hydrogen peroxide production via ORR[50] and nitrogen reduction reaction (NRR),[51] have also attracted a lot of research interest.

A good catalyst should have a balanced binding energy to the reactant, intermediates and product involved in a catalytic process so that reactant can be strongly adsorbed and activated, meanwhile the product binds weakly and can be easily desorbed from catalyst surface. The concept of an optimal catalyst is well illustrated in the Sabatier principle, as shown in **Fig. 8A**, where the desired catalysts sit at the peak of the "volcano plot" referred to as a "hot spot" for catalysis.[52]

In the case of reactions where only one intermediate is involved (e.g. HER/HOR) the volcano plot provides a simple yet comprehensive model for understanding the fundamentals of catalysis. An active catalyst is required to have a near-equilibrium binding energy to H* (* stands for a catalytically active site that binds to the absorbate), as understood from the density functional theory (DFT) calculations (**Fig. 8B)**.[53] Platinum group metals (PGM), including Pt, Re, Pd, Rh and Ir are the best monometallic catalysts for HER as they are adjacent to the apex of the volcano plot (**Fig. 8C**), where ΔG is the calculated Gibbs free energy of H* adsorption at potential U = 0 V.[54] H* adsorption is the only but an effective descriptor for predicting catalyst activity towards HER, and thus the free energy diagram correlates well with the volcano plot. As a simple and straightforward guideline for discovering new catalysts, this model works effectively in explaining the experimental results

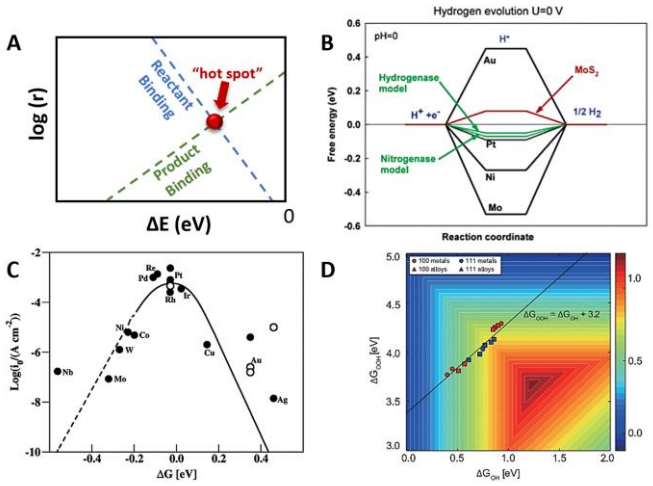

Fig. 8: (A) Schematic of the Sabatier principle for catalysis in general, **(B)** calculated free energy diagram for HER at a potential U = 0 relative to the standard hydrogen electrode at pH = 0 (Reprinted from ref. 53 with permission, Copyright 2005 American Chemical Society), **(C)** volcano plot of measured exchange current density plotted versus the calculated free energy of H adsorption at U = 0 V. The metals on the left side of the volcano have high H coverage (1 ML) and the metals on the right side have low H coverage (0.25 ML). The line is a prediction by a kinetic model in which all input parameters are taken from DFT calculations. The dashed line indicates that the metals which bind H stronger than 0.2 eV/H usually form oxides at U = 0 V. The open circles are (111) facet data whereas the filled circles are polycrystalline (Reprinted from ref. 54 with permission, Copyright 2010 American Chemical Society), and (D) calculated limiting potential (the potential where an overall electrocatalytic reaction becomes endergonic) for ORR (Reprinted from ref. 56b with permission, Copyright 2015 Oxford University Press).

and predicting the trend of catalyst activity, especially in the case of HER, yet it disregards the factors of absorbate coverage, solvent effects and kinetics. In the overall hydrogen catalysis, $H_2 \leftrightarrow 2H^+ + 2e^-$, Pt reversibly catalyzes both HER and HOR at negligible overpotential in acidic condition. In contrast, the HER/HOR catalysis on Pt in alkaline condition requires a more significant overpotential.[55] The volcano plot successfully explains why Pt is superior to other catalysts for hydrogen catalysis but fails to give any insights into the different performance in different pH conditions. The "optimal catalyst" at the apex of a volcano plot is a hypothetical point. Experimentally, the best catalyst may not sit at the apex due to certain limits in preparing a catalyst surface.

The volcano plot with a single descriptor is not sufficiently effective in determining the trends of catalytic activity and selectivity for catalysis involving multiple intermediates. Although a catalyst surface can be tuned towards an optimal adsorption energy for one specific intermediate that is involved in a rate-determining step, its binding strength to related intermediates is strongly correlated and is unable to be de-coupled due to the "scaling relationship". In the case of ORR catalysis on a Pt surface, OOH* adsorption energy has a nearly linear relationship to OH* adsorption energy on different facets of Pt and Pt-based alloy catalysts, as shown in **Fig. 8D**. OOH* binds weakly to Pt surface and OH* binds strongly to Pt surface. Ideally, it is most favored to enhance the binding of OOH* and simultaneously weaken the binding of OH*, but this is forbidden on a single-component catalyst surface due to the strongly coupled scaling relationship. How to break the scaling relationship between multiple intermediates on a catalyst surface is a cutting-edge research frontier. Strategies such as creating strains to favor different absorbate at different catalyst sites[56], introducing a second catalyst site to the primary catalyst site[57] and using a combination of cascade/tandem catalysts to favor the adsorption of various adsorbates onto different catalyst sites, have been recently developed for different catalytic reactions.[58] In those cases, the basic concept is to have one intermediate generated at the first catalytic site, followed by the "spillover" of the intermediate to a second catalytic site that favors different steps of the reaction.

The development of efficient catalysts can be realized by maximizing the catalytically active sites and/or enhancing the intrinsic activity of a catalyst surface. With well-defined size, morphology, shape/facet control and component stoichiometry, monodisperse NPs are ideal subjects for studying and identifying active sites for catalysis.

Fuel Cell Electrocatalysis

Oxygen reduction reaction (ORR) catalysis has been one of the most intensively studied topics because it is the rate-determining step that limits the overall energy conversion efficiency of fuel cells and batteries.[59] The state-of-the-art single-component catalyst for ORR is Pt. However, Pt binds to oxygenated species (O*) over strongly compared to the optimal value in volcano plot, as shown in **Fig. 9A.**[60] Monodisperse Pt NPs have been synthesized and tested for ORR. In $HClO_4$ solution, it was found that Pt NPs about ~2.2 nm had the highest mass activity (activity normalized to Pt weight) and specific activity (activity normalized to the surface area).[61] The facets exposed at the surface of NPs are also paramount; Pt (111) facet is the most active facet in $HClO_4$ solution towards ORR, while (110) and (100) facets are much more active in H_2SO_4 solution.[62] This acid-induced catalysis change on different crystal facets is attributed to the anion interaction with Pt surface. For example, in a strongly absorbing electrolyte, such as sulfuric acid, Pt (100) and (110) facet are relatively more active due to the strong tridentate bond of SO_4^{2-} to the (111) facet.[63] An alternative strategy is to alloy Pt with another non-noble metal to introduce electronic (ligand), strain (geometric) and ensemble (coordination) effects.[64] All of these fundamental studies require to have monodisperse NPs as the catalyst so that catalytically active/selective surface can be better identified for catalysis optimization.

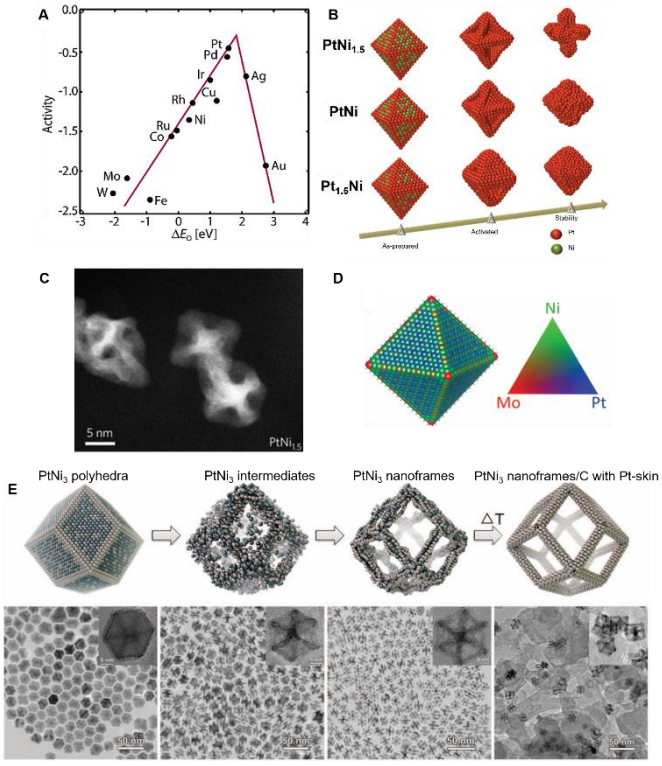

Figure 9: (A) Trends in oxygen reduction activity plotted as a function of the O* adsorption energy (Reprinted from ref. 60 with permission, Copyright 2004 American Chemical Society), **(B)** schematic representation of the PtNi nano-octahedra with different compositions morphology and surface structure changes after electrochemical surface activation (25 potential cycles) and electrochemical stability tests relative to as-synthesized NPs, **(C)** STEM image of $PtNi_{1.5}$ concave octahedra after 25 potential cycles, suggesting leaching of the Ni component (B and C are both reprinted from ref. 65a with permission, Copyright 2013 Springer Nature), **(D)** $Mo_{73}Ni_{1143}Pt_{3357}$ NPs at 170°C as determined by Monte Carlo simulation. Occupancies are indicated by the color triangle on the right. Small spheres represent the atoms in the outer layer (Reprinted from ref. 66 with permission, Copyright 2015 The American Association for the Advancement of Science), **(E)** schematic illustrations and corresponding TEM images of the samples obtained at four representative stages during the evolution process from polyhedral to nanoframes (Reprinted from ref. 67 with permission, Copyright 2014 The American Association for the Advancement of Science).

An intensively studied system is octahedral PtNi NPs with the surface being exclusively the (111) facet, which has been demonstrated as very active for ORR in $HClO_4$ (**Fig. 9B**).[65] However, Ni in the NiPt structure is not stable, leaching out preferentially near the center of the (111) facet during ORR catalysis in acidic condition, as a result, the shape of $PtNi_x$ may evolve into concave structures as illustrated in **Fig 9C** and further into multipods. The Pt-rich $Pt_{1.5}Ni$ better maintained the (111) facet after the electrochemical leaching of Ni compared to the Ni-rich $PtNi_{1.5}$, which contributed to increased activity in the etched structure. The structural evolution of the shape-controlled NPs complicates ORR catalysis, suggesting the importance of maintaining the shape as well as the catalytic components.

To further enhance the ORR catalysis, transition-metal doping strategies have been applied to the PtNi octahedra.[66] The doping was accomplished by seed-mediated growth of the transition-metal on the PtNi octahedra with metal carbonyl precursors. Cr-, Fe-, Co-, Mo-, Re- and W-doped Pt_3Ni octahedra showed superior mass activity to the seed NPs. Mo-doped Pt_3Ni demonstrated a specific activity of 10.3 mA/cm^2 and mass activity of 6.98 A/mg_{Pt} in O_2-saturated 0.1 M $HClO_4$ at room temperature. A modeling study showed that Mo has a strong driving force to segregate at the surface, preferentially occupying the vertices and edges connecting adjacent (111) facets (**Fig. 9D**). The surface-segregated Mo stabilizes Pt and Ni against dissolution, thus enhancing the stability of PtNi octahedra in ORR condition. In another case, structural evolution of shape-controlled PtNi NPs was found to lead to three-dimensional porous structure that is highly active towards ORR.[67] $PtNi_3$ rhombic dodecahedra NPs were synthesized in oleylamine and slowly transformed into porous nanoframes, as shown in **Fig. 9E**. The structural evolution from electrochemical leaching was also found in the ultrathin PtNi nanowires. The core/shell Pt/NiO nanowires slowly transformed into rough-surfaced Pt nanowires with trace amount of Ni left in the core.[68] The de-alloyed PtNi nanowires showed an unprecedentedly high activity towards ORR in 0.1 M $HClO_4$ at room temperature. The modeling study showed that the de-alloyed PtNi nanowires possess a large portion of undercoordinated surface and the Pt-Pt bond is compressed, resulting in ensembles similar to Pt (111) facet.

Despite their impressive ORR activity demonstrated in 0.1 M $HClO_4$ at room temperature, the proton exchange membrane fuel cells operate at 80 °C and the catalysis occurs at a solid-liquid-gas three-boundary interface which is not often studied and those tested in the membrane electrode assembly (MEA) condition did not show much impressive and consistent catalysis enhancement compared to the commercial Pt. The best fuel cell performance was demonstrated on de-alloyed ~ 5 nm PtNi NPs showing improved durability.[69] However, the acid-pretreated PtNi NPs still suffered from significant loss of Ni component after 30,000 cycles in fuel cell test with only ~4-15% Ni remaining.

Intermetallic NPs, specifically $L1_0$-structured (tetragonal) NPs, have provided an effective approach to stabilize Pt-based alloys in corrosive fuel cell conditions.[70] 9 nm MPt (M = Fe, Co)

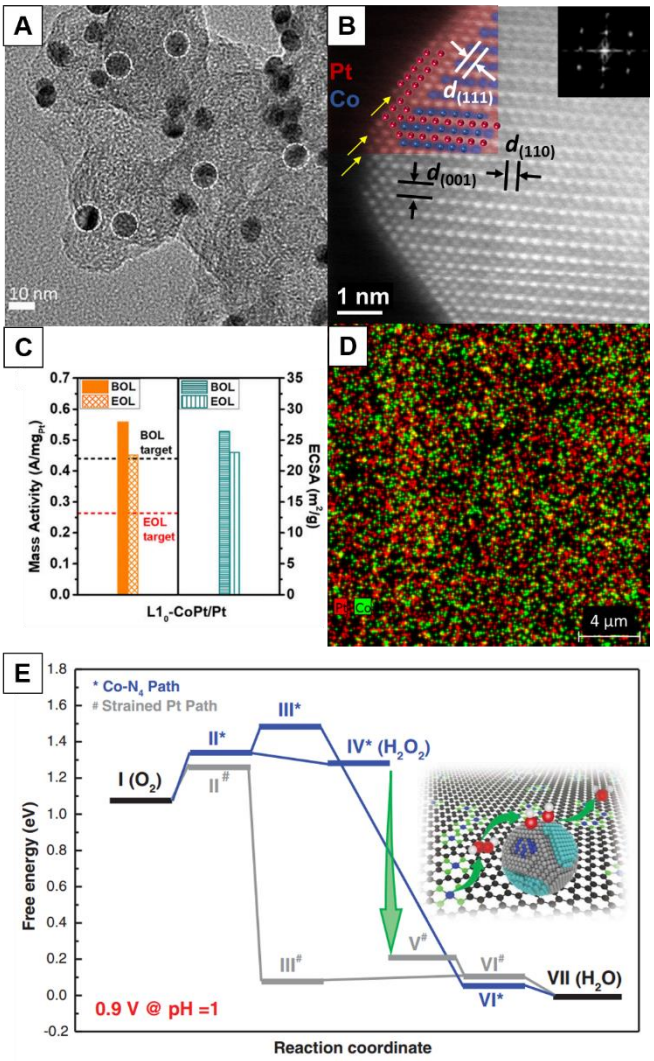

Figure 10: (A) TEM image of the C-CoPt NPs after annealing to form a spherically-shaped NP, **(B)** HAADF-STEM image of core/shell $L1_0$-CoPt/Pt NPs with 2–3 atomic layers of Pt shell over $L1_0$-CoPt core before the durability test, **(C)** Mass activities of tested $L1_0$-CoPt *via* the current DOE protocol compared with activity targets of the DOE, **(D)** elemental mapping of a large-area of the MEA assembled with $L1_0$-CoPt/Pt NPs after durability test in MEA at 80 °C (A-D are all reprinted from ref. 71 with permission, Copyright 2019 Elsevier), **(E)** Free-energy diagram of the ORR pathways. The proposed associative reaction coordinates represent the following states: (I) * or # + O_2 + 4H$^+$ + 4e$^-$, (II) OOH* or OOH# + 3H$^+$ + 3e$^-$, (III) O* or O# + H_2O + 2H$^+$ + 2e$^-$, (IV) * + H_2O_2 + 2H$^+$ + 2e$^-$, (V) 2OH# + 2H$^+$ + 2e$^-$, (VI) OH* or OH# + H_2O + H$^+$ + e$^-$, and (VII) * or # + 2H_2O, where * (blue) denotes the binding site on Co-N_4 embedded in graphene and # (gray) denotes the binding site on a strained Pt (111) facet. (Inset) Schematics of H_2O_2 generated over Co-N_4 migrating to the strained Pt (111) surface (green arrows), followed by dissociation to OH# and water formation (Reprinted from ref. 74 with permission, Copyright 2018 The American Association for the Advancement of Science).

with $L1_0$-structured core and a compressively strained Pt shell with 2-3 atomic layers (**Fig. 10A,B**) were found to effectively stabilize M in the MEA condition of 80 °C.[71] The intermetallic NP catalyst showed high activity before and after catalysis, respectively, as seen in **Fig. 10C**, while maintaining the composition of M at ~40% after 30,000 cycles of a durability test across the MEA electrode which was imaged after (**Fig. 10D**). This activity and stability beat the DOE 2020 targets of 0.44 A/mg_{Pt} and less than 40% loss after 30,000 cycles in mass

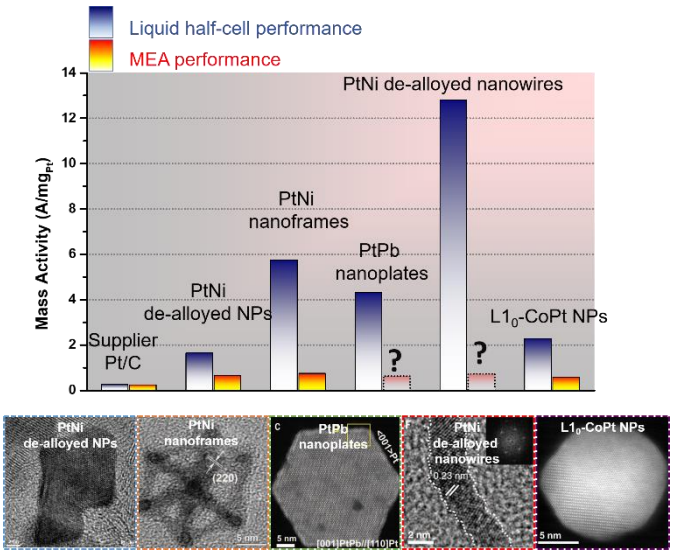

Fig. 11: ORR mass activity of representative NPs catalyst systems collected in liquid half-cell at room temperature and in MEA at 80 °C. The data points and corresponding TEM and HAADF-STEM images are reprinted from ref. 65a (With permission, Copyright 2013 Springer Nature) and ref. 69 (Published by The Royal Society of Chemistry) for PtNi de-alloyed NPs, ref. 67 (With permission, Copyright 2014 The American Association for the Advancement of Science) for PtNi nanoframes, ref. 73 (With permission, Copyright 2016 The American Association for the Advancement of Science) for PtPb nanoplates, ref. 68 (With permission, Copyright 2016 The American Association for the Advancement of Science) for PtNi de-alloyed nanowires and ref. 71 (With permission Copyright 2019 Elsevier) for L1$_0$-CoPt NPs.

activity.[72] Due to smaller lattice constants of L1$_0$-CoPt compared to L1$_0$-FePt, the Pt shell in the L1$_0$-CoPt/Pt structure is compressed further (-4.50%/-4.25% biaxial strain), binding more weakly to oxygenated species and thus exhibits higher ORR activity. PtPb nanoplates were also synthesized to form an intermetallic structured core (hexagonal) surrounded by Pt shell, showed an excellent mass activity of 4.3 A/mg$_{Pt}$.[73] It also demonstrated very stable ORR performance up to 50,000 cycles in 0.1 M $HClO_4$ at room temperature, yet Pb still suffered from leaching problem (from ~48% to ~15%) in the structure after the durability test.

Using the concept of cascade catalysis, CoPt NPs were incorporated into another catalytic site, Co-N-C material, which was derived from Co- and Zn-containing metal organic framework (MOF).[74] The MOF was first synthesized and subsequently loaded with Pt precursor. The Co component from the MOF serves as the precursor to alloy with Pt during high-temperature reaction to form CoPt NPs. This catalyst achieved a mass activity of 1.77 A/mg$_{Pt}$. The DFT calculations showed that the Co-N_4 catalyst site favors the 2 electrons-pathway by forming H_2O_2 with a relatively low overpotential (**Fig. 10E**). The generated H_2O_2 can easily desorb and migrate to adjacent CoPt NPs, subsequently being reduced to H_2O by PtCo via a thermodynamically spontaneous step. The synergistic catalysis can thus bypass the strongly bonded O* and OH* intermediates on Pt surface, resulting in an overall enhanced ORR catalysis. However, assigning all catalytic activity to Pt may underestimate the catalyst performance when calculating the mass activity as the Co-C-N catalyst sites also showed activity in fuel cells.[75]

The novel NP catalysts have greatly advanced the ORR catalysis and fuel cell applications. Nevertheless, a huge gap exists between the screening process of the ORR catalysts in either $HClO_4$ or H_2SO_4 electrolyte via the liquid half-cell test and the device applications via the MEA test. Some representative catalyst systems are summarized in **Fig. 11**, illustrating also the commercial Pt NPs supported on carbon.[64] The discrepancy in different testing conditions implies that the current rotational disk electrode (RDE)-based liquid half-cell test may overestimate the ORR activity of Pt-based alloy NPs. The possible reasons for this discrepancy are: (1) oxygen diffusion and water product removal is a common issue at the three-boundary interface of the catalyst layers in MEA, while in the thin film working electrode tested in liquid half-cell oxygen can be easily accessible and products are efficiently removed via rotation; (2) catalyst layer uses perfluorosulfonic acid ionomer as electrolyte, but the electrolyte used in these RDE tests shown in **Fig. 11** is $HClO_4$, which has negligible bonding to Pt surface and thus Pt surface is more accessible to reactants and intermediates; (3) MEA condition of 80 °C is harsher than the RDE test performed at room temperature, resulting in possible leaching of non-precious components in Pt-based alloy NPs and possible shape evolution which makes them behave more like pure Pt catalysts with no structural control. As the MEA test is time-consuming and expensive, more fundamental studies on the proper and rapid screening test should be conducted to understand this performance gap. For the synthetic control of NP catalysts, robust NPs with preferred surfaces should be further developed. To better understand the ORR catalysis of NPs, as well as other relevant fuel cell reactions, the structure, morphology and composition of NPs should be assessed carefully with advanced *in-situ* and *ex-situ* techniques during the reaction.

Electrochemical Reduction of CO_2

The selective conversion of CO_2 to an active form of carbon has been one of the most widely studied problems in the past decade and using monodisperse NP catalysts has come about as one of the possible solutions to increase reaction activity and selectivity. In 1985, Hori used Cu as the catalyst to electrochemically reduce CO_2 to hydrocarbons like methane and ethylene in one-step under ambient conditions (room-temperature and pressure) in aqueous solutions.[76] In this method, electricity serves as the energy source, with the possibility to be generated by renewable sources like wind and solar, and H_2O and CO_2 act as the renewable hydrogen and carbon sources, which is ideal for greener CO_2 conversion processing.[77] The fast development of NP synthesis has made it possible to study in more detail the CO_2 reduction reaction (CO_2RR) mechanism,[78] especially for the CO_2RR to CO on a Au surface.[79] To reveal what sites on the catalyst surface that are active and selective for the CO_2RR to CO, stable monodisperse Au NPs were prepared and studied.[80] Monodispersed Au NPs with the diameter of 4, 6, 8 and 10 nm were prepared through the burst nucleation method (using a strong reducing agent). Among Au NPs catalysts with different sizes, 8 nm Au NPs showed the best CO_2 reduction activity for the formation of CO; the faradaic efficiency (FE) reached 90% at -0.67 V vs. RHE (**Fig.**

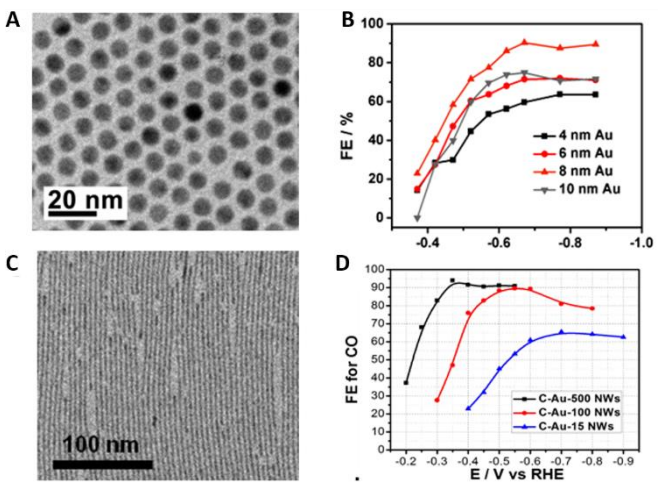

Fig. 12: (A) TEM image of monodisperse 8 nm Au NPs , **(B)** the reduction potential-dependent faradaic efficiency (FE) of CO formation from CO_2 electroreduction over Au NP catalysts (A and B reprinted from ref. 80 with permission, Copyright 2013 American Chemical Society), **(C)** TEM image of 500 x 2 nm Au nanowires, and **(D)** the reduction potential dependent FE for CO formation from CO_2 electroreduction in 0.5 M $KHCO_3$ over different lengths of Au nanowires (C and D reprinted from ref. 81 with permission, Copyright 2014 American Chemical Society).

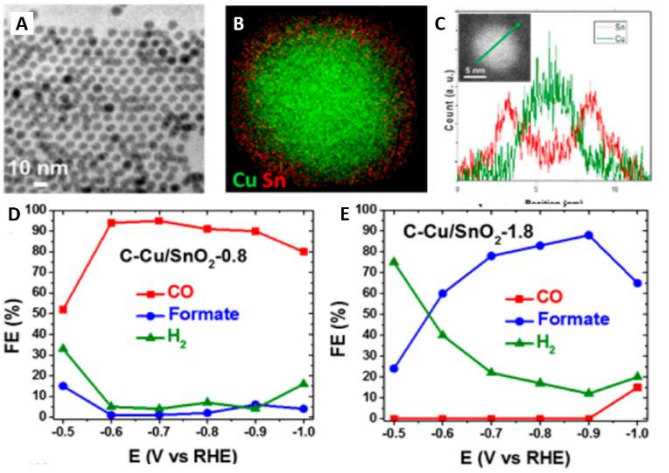

Fig. 13: (A) TEM image of 7/0.8 nm core/shell Cu/SnO_2 NPs, **(B)** EELS elemental mapping on one 7/0.8 nm Cu/SnO_2 NP, and **(C)** EELS line scan of one 7/0.8 nm Cu/SnO_2 NP. Electrochemical CO_2 reduction results for product formation of CO, formate, and H_2 of **(D)** C-7/0.8 nm Cu/SnO_2 NPs and **(E)** 7/1.8 nm Cu/SnO_2 NPs. Images reprinted from ref. 33b with permission, Copyright 2017 American Chemical Society.

12A,B). Density functional theory (DFT) calculations highlighted that 8 nm Au NPs have the best activity because their crystal domain has the largest edge/corner ratio and the edge site is most active site for CO formation. With the observation and calculation from monodispersed Au NPs of this favoured facet configuration, the work was extended to the synthesis of monodispersed 2 nm ultrathin Au nanowires of different lengths as seen in **Fig. 12C**.[81] This synthesis was chosen due to the abundance of edge sites on the ultrathin Au nanowires. After electrochemical CO_2 reduction under the same conditions (0.1 $KHCO_3$ aqueous solution and CO_2 bubbling), the 500 nm long ultrathin Au nanowires produced CO with a FE of 94% at -0.35 V vs RHE, which shows higher FE and lower overpotential than 8 nm Au NPs seen clearly in **Fig. 12D**. The increased activity and selectivity was explained by the larger edge/corner ratio in the longest ultrathin nanowires compared with the shorter nanowires and also the NPs. Using monodispersed NPs to investigate the active site of CO_2 electroreduction and further improve their activity has also been pursued on other NPs, such as Ag and Pd, and demonstrate an exciting direction in the optimization of NP catalysts for the CO_2RR.[82]

Core/shell architecture and control in NP composition has also been applied to create new catalysts for CO_2RR. The effect of the inner core has been seen to affect the overall reaction selectivity and activity, as demonstrated in the Cu/SnO_2 core/shell NPs with 0.8 nm or 1.8 nm SnO_2 shell as catalysts for CO_2 electroreduction (**Fig. 13A-E**).[33b] Even though the thickness of the SnO_2 shell only changes 1 nm from 0.8 nm to 1.8 nm, the selectivity of the CO_2 reduction products is changed from CO to formate. DFT calculation suggested that trace amount of Cu could diffuse into the 0.8 nm SnO_2 shell and affect the lattice strain of SnO_2 shell. A similar effect has been seen through the construction of monodisperse Cu/In_2O_3 core/shell NPs, but the focus was on tuning CO formation through altering the In_2O_3 shell and CO_2RR reduction potentials.[83] Such a core/shell architecture was further extended to other systems, such as Ag/Sn bimetallic catalyst for selective formation of formate.[84]

Compared with stable noble metal NP catalysts, Cu catalysts have shown great promise as a way to access hydrocarbons. However, pure Cu NPs are unstable and poorly selective.[86] To stabilize Cu, monodisperse AuCu NPs were prepared and studied for CO_2RR to CO.[86] Alloying Cu with Pd yielded comparable selectivity to CO as did alloying with Au.[87] Beyond alloying, monodispersed 7 nm Cu NPs assembled on pyridinic-N rich graphene (p-NG) showed reduction potential dependent selectivity to formate at -0.8 V, but C_2H_4 at -0.9V or beyond.[88] Because of the ability of p-NG to act as a CO_2 and proton absorber, combined with synergistic Cu activity for hydrogenation and C-C coupling, the composite structure was much more active and also stable than pure Cu NPs for CO_2 electroreduction. Recently, shape within monodispersed Cu NP catalysts was explored to tune CO_2RR. Cu NWs have been synthesized through various methods and have been able to change the hydrocarbon selectivity of Cu based on morphological features of the NWs.[89] For example, when ~20 nm in diameter Cu NWs were tested for the CO_2RR, 55% FE for methane production was achieved, and this FE was shown to change throughout the reaction, beginning to form a notable amount of ethylene, due to the morphology change of the NWs with potential. When the Cu NWs are 50 nm in diameter with a larger fraction of (100) facets exposed, a FE of 60% for C2 hydrocarbons (C_2H_4 and C_2H_6) were obtained from CO reduction. CO_2RR selectivity on these NWs was lower due to the CO_2RR to CO conversion required for C2-product formation. One new strategy has been to couple two different metals together in cascade/tandem catalysts, one that has selectivity toward forming CO and the other which can transform CO to hydrocarbons, which until now the latter has been Cu.[90] An example of this has been studied on coupling Au and Cu, to act as a bifunctional catalyst to improve FE to different kinds of hydrocarbons.[90c]

Green Chemistry Applications of Monodisperse NPs

Green chemistry refers to the reduction of hazards and waste associated with chemical synthesis and applications. The twelve principles of green chemistry were first established to offer guidelines on what it means for a chemical, a process, or a procedure to be "green."[91] Within these twelve principles have arrived countless new research directions, many centred around one of the twelve principles: *catalysis*. To make a chemical conversion more sustainable, catalytic reactions are preferred compared to those conversions with stoichiometric reagents and chemical additives.

Using NPs as catalysts for chemical conversions can be more advantageous than homogenous catalysis. Supported NP catalysts can easily be separated from the reaction mixture through filtration, centrifugation, or coupling with a magnetically-separable component allowing for easy catalyst reuse and isolation of the products of the reaction.[92] Further, with advances in NP synthesis, catalysts can be optimized either through adding a bifunctional component to the catalyst or intrinsically changing the activity of the active component.

Two of the primary principles of conducting green chemistry are providing less hazardous chemical syntheses as well as creating inherently safer conditions, both to the researcher and to the environment. When thinking of a common hydrogenation reaction, conventional approaches utilize high-pressure hydrogen (H_2) cylinders as a source of H_2 for the reaction often combined with high-pressure reaction set-ups. Monodisperse NP catalysed dehydrogenation of small hydrogen storage molecules is considered a green chemistry alternative to hydrogenation for on-site or *in-situ* formation of H_2.

Of the H_2 sources considered, ammonia borane (AB) is particularly interesting and widely studied because of its high weight percent hydrogen (19.5%) and stability under standard conditions.[93] Further, it is not flammable or toxic, making it a possible green alternative to other reductants such as sodium borohydride ($NaBH_4$) or Lindlar's catalyst which employs lead or quinoline as a catalyst poison.[94] AB can undergo catalytic hydrolysis or methanolysis to release 3 mol H_2 for every 1 mol of AB. Monometallic metal NP catalysts (Pt, Pd, Ru, Cu, Ni) have been developed to release H_2 from AB through AB hydrolysis or methanolysis,[95] and such progress has been reviewed recently.[96] In an effort both to stabilize NPs against leaching, as well as increase the activity of NP catalysts, there have been many works trying to develop bimetallic and even trimetallic NP systems to optimize AB dehydrogenation (CoPd, FePd, PtPd, CuPt, CoPt, NiPt).[97] Alloying non-noble metals like Cu and Ni in monodispersed 16 nm CuNi NPs, or others, has also improved catalyst stability and activity.[98] Efforts have also been made immobilizing monodisperse NPs on robust supports to further combat stability issues. For example, Ni NPs supported on molybdenum disulphide (MoS_2) were demonstrated to effectively produce H_2 from AB, while also being very stable.[99]

In addition to AB, formic acid (FA) is also a promising H_2-storage molecule. FA, a product of biomass decomposition, undergoes catalytic decomposition to form gaseous products (CO_2 and H_2 via a direct dehydrogenation pathway, and sometimes CO via a dehydration pathway).[100] Monodispersed bimetallic Pd-based NP alloys such as 3.8 nm AuPd and 2.2 nm AgPd were prepared and found to increase the activity of NPs for the decomposition of FA under mild conditions (1 atm, 50 ˚C), without the formation of CO.[101] Interestingly, surface control of AgPd NPs to create alloys with varying surface exposure of Pd atoms have been used as a CO_2 hydrogenation catalyst to form FA under moderate conditions (20 atm, 100 ˚C), highlighting a potentially reversible process in which CO_2 and H_2 produced from FA decomposition and not used in a tandem process can be reused.[102] Similar to AB dehydrogenation, support interactions have been utilized to increase the activity of FA dehydrogenation. 3.3 nm Au NPs supported on Al_2O_3 and 1.8 nm Au NPs supported on ZrO_2 have also been shown to decompose FA under mild conditions, with the primary source of stability and activity coming from the metal-support interactions.[103] Pd coupled with pyridinic-N-doped carbon, NiPd or AuPd on NH_2-functionalized and N-doped reduced graphene oxide, and AgPd coupling with oxygen-deficient tungsten oxide ($WO_{2.72}$), among others have all been utilized to maximize activity and stability.[104] The creation of NPs with a core-shell architecture has also proved to be valuable for improving FA decomposition.[105] For example, monodispersed 7.3 nm core/shell Au/Pd NPs boosted catalytic activity due to localized surface plasmon resonance (LSPR) effects of Au on Pd.[105b]

The NP catalysts active for H_2 generation from AB or FA are often active for catalysing hydrogenation reactions under mild conditions, making these NPs an attractive class of new catalysts for tandem reactions. In the past decade, tandem catalysis (also referred to as domino catalysis or one-pot catalytic reactions) has been gaining popularity in organic syntheses to minimize reactant, solvent, and potentially even catalyst waste. The theory has been reviewed recently, focusing on optimizing multiple reaction conditions.[106] Tandem catalysis for the one-pot production of H_2 from AB over monodispersed 3.3 nm NiPd NPs and hydrogenation of nitro/nitrile compounds was demonstrated at room temperature and ambient pressure.[18a] Such tandem reactions could proceed well on many Pd-based catalysts such as shape-controlled AuPd nanorods (AB hydrolysis/4-nitrophenol reductions), CoPd NPs ($NaBH_4$ hydrolysis/nitro group reduction), CoPd NPs (AB hydrolysis/nitro, nitrile, carbonyl group reduction), among others.[107]

Beyond nitro/nitrile reductions, tandem NP catalysis has been extended to prepare n-heterocyclic rings such as benzoxazoles and quinazolines in greener chemistry conditions. One-pot reactions of FA, 2-nitrophenol, and aldehydes formed benzoxazoles with near quantitative yields over the monodispersed 2.2 nm AgPd NPs (**Fig. 14A**) coupled with oxygen-deficient tungsten oxide ($Ag_{48}Pd_{52}/WO_{2.72}$).[104a] The NPs after coupling can be seen in **Fig. 14B**, along with a cartoon schematic (**Fig. 14C**). The control of NP composition was achieved through co-reduction of the silver and palladium precursors in the presence of oleylamine and reducing agent; the assembly with $WO_{2.72}$ was achieved through the growth of AgPd in the presence of preformed $WO_{2.72}$. Monodisperse NP

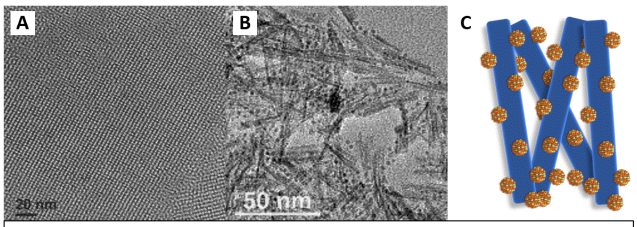

D

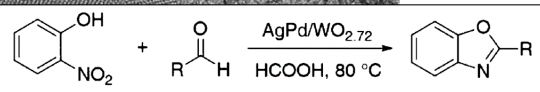

entry	R	yield (%)	entry	R	yield (%)
1	Ph	99	4	4-F-Ph	95
2	4-Me-Ph	99	5	4-CN-Ph	98
3	4-OMe-Ph	99	6	cyclohexyl	83

E

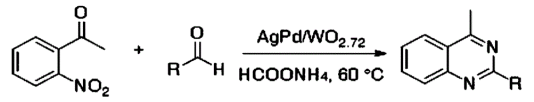

entry	R	yield (%)	entry	R	yield (%)
1	Ph	99	4	4-F-Ph	92
2	4-Me-Ph	96	5	4-CN-Ph	99
3	4-OMe-Ph	93	6	cyclohexyl	88

Fig. 14. (A) TEM image of 2.2 nm $Ag_{48}Pd_{52}$ NPs, **(B)** TEM image of the assembly of AgPd NPs on oxygen-deficient tungsten oxide ($WO_{2.72}$), **(C)** cartoon schematic of the AgPd/$WO_{2.72}$, composite structure, **(D)** catalytic results for the tandem dehydrogenation of FA and formation of benzoxazoles, and **(E)** catalytic results for the tandem dehydrogenation of ammonium formate and formation of quinazolines. Figures reprinted from ref. 104a with permission, Copyright 2017 American Chemical Society.

synthesis and assembly on the $WO_{2.72}$ nanorods was optimized as a universal catalyst to use H_2 formed *in-situ* from FA or ammonium formate (AF) to form a library of value-added n-heterocyclic products under mild conditions, 1 atm, 50-80 ˚C (**Fig. 14D-E**). $WO_{2.72}$ was also used to support monodispersed Cu NPs and improve their catalytic activity for AB dehydrogenation and stability for tandem selective hydrogenation of nitrostyrene.[108]

Looking to the future of tandem catalysis, stabilization of NPs is paramount as the reaction conditions of each part may be very different, and the catalyst itself must be robust to perform universally well while being reusable. Zeolite-matrix and polymer stabilized monodisperse NPs have risen as possible materials to add to NP stability.[109] Further, another advantage of monodisperse NPs is their ability to create uniform monolayer assemblies[110] which can maximize the surface available for catalysis.[111] In a recent demonstration, monodispersed 3 nm NiPd NPs were prepared and assembled on a solid substrate via the transfer of a monolayer assembly (**Fig. 15A-C**).[18b] Combined with pre-deposition of a monolayer of nitrogen-doped graphene (NG), a composite structure containing a monolayer of NiPd NPs on a monolayer of NG could be fabricated on a silica or glass substrate. This monolayer composite can serve as a catalyst probe, actively controlling reactions process and minimizing the work-up procedures for product separation as demonstrated in one-pot hydrolysis of AB, nitro-reduction, and quinazoline synthesis under mild conditions (1 atm and 60 ˚C) (**Fig. 15D**); the reaction set-up in

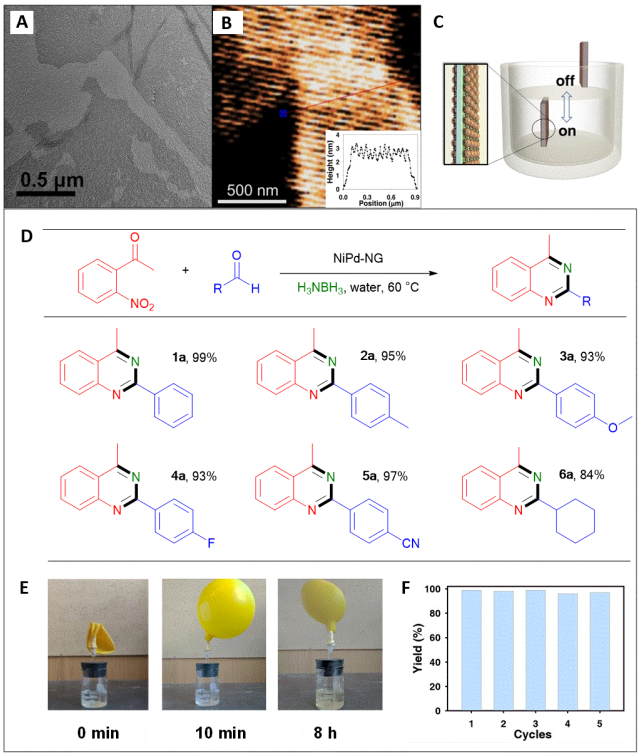

Fig. 15. **(A)** TEM image of a monolayer of NiPd on monolayer nitrogen-doped graphene, **(B)** atomic force microscopy (AFM) image of monolayer NiPd on monolayer nitrogen-doped graphene on a silica substrate, **(C)** general schematic highlighting the assembly of a catalyst probe that is easily reusable and removed from the catalytic reaction, **(D)** catalytic results for the dehydrogenation of AB and tandem formation of quinazolines, **(E)** reaction set-up where the ballon captures H_2 formed *in-situ*, and **(F)** catalyst activity for the formation of quinazoline after being recycled. Figures reprinted from ref. 18b with permission, Copyright 2018 John Wiley & Sons, Inc.

Fig. 15E highlights the production of H_2 in a balloon that would transfer to the following hydrogenation and other ring-closure reactions for the formation of quinazolines. The catalyst probe was stable for the tandem reactions, showing no obvious activity drop in 5 rounds of reaction tests (**Fig. 15F**). Such an assembly approach highlights a potential future direction in green chemistry applications of NP catalysts with maximum NP surface exposure for catalytic enhancement and optimization.[112]

Monodisperse NPs also show great potential as catalysts in biomass conversion. General NP catalysts for this application have been reviewed recently.[113] Still, the development of catalysts to transform these platform chemicals to value-added chemicals is an ongoing research field. Levulinic acid (LA) and its ester derivatives, furfural, as well as FA are all platform chemicals that can arise from biomass decomposition.[114] Much work has tried to convert LA to gamma-Valerolactone (GVL),[115] or similarly to pyrrolidones .[116] Recently, AuPd and supported Pt NP catalysts have demonstrated successful conversion of LA to libraries of pyrrolidones under the mild reaction conditions at 85 °C and 1 atm H_2. Monodisperse 3.8 nm alloy $Au_{66}Pd_{34}$ NPs (**Fig. 16A-C**) were synthesized through co-reduction.[19c] The AuPd alloys performed much better activity and stability for the

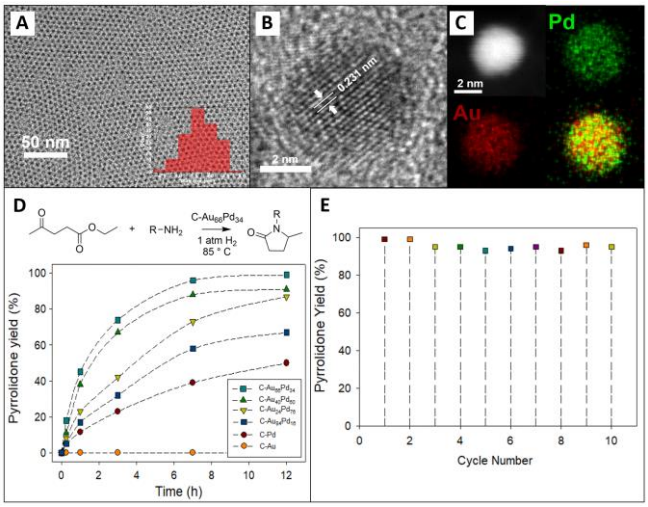

Fig. 16: (A) TEM of 3.8 nm $Au_{66}Pd_{34}$ NPs, **(B)** high-resolution TEM image of one $Au_{66}Pd_{34}$ NP, **(C)** elemental mapping of one $Au_{66}Pd_{34}$ NP showing alloy distribution of the two components, **(D)** catalytic activity of different compositions of AuPd alloy NPs for the reductive amination of ethyl levulinate with octylamine under 1 atm H_2, and **(E)** stability measurements for successive runs of the reductive amination of ethyl levulinate with octylamine over the same C-$Au_{66}Pd_{34}$. Figures are reprinted from reference 19c with permission from The Royal Society of Chemistry.

tandem nucleophilic addition and hydrogenation than pure Pd or Au NPs for the formation of pyrrolidones (**Fig. 16D-E**). Coupling Pt NPs with porous titania (p-TiO_2)(**Fig. 17A-C**) is

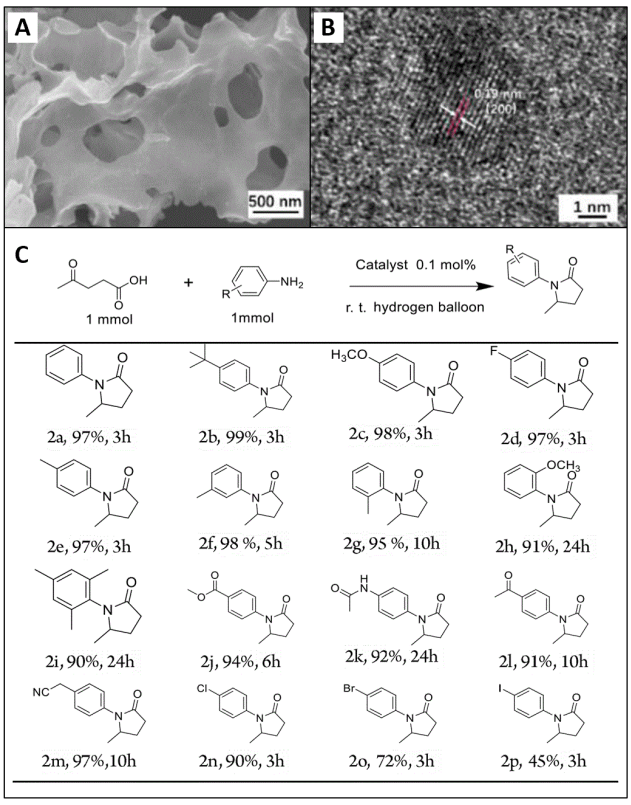

Fig. 17: (A) SEM image of porous titania nanosheets (p-TiO_2), **(B)** HR-TEM of 1.8 nm Pt NP on p-TiO_2 support, and **(C)** catalytic activity at room temperature and 1 atm H_2 pressure for a series of substrates for the reductive amination of LA. Images are reprinted from ref. 117 with permission, Copyright 2019 American Chemical Society.

another approach to create a better catalyst for the reductive amination of LA or its esters.[117] In both AuPd and Pt-p-TiO_2 structures, the catalytic active Pd and Pt sites become "electron deficient" due to Au alloying and strong Pt-TiO_2 coupling effects, creating favourable electronic environments to avoid higher pressure and temperature reactions for biomass conversion that have previously been reported.[116] Therefore, tuning interparticle interactions as well as NP-support interactions are benefits of optimizing catalysis with monodisperse NPs.

Beyond these, monodisperse NP catalysts have also been demonstrated to enhance catalysis for other organic reactions,[118] including C-C coupling reactions.[119]

Monodisperse NPs for Nanomedicine

Nanomedicine encompasses the applications of nanotechnology to the field of medicine.[120] In particular, NPs have been widely investigated for cancer diagnosis and therapy. These applications are feasible because long-circulating NPs can selectively accumulate in tumours via the enhanced permeability and retention (EPR) effect.[121] The tumour targeting and retention can be improved by coupling a targeting ligand to NPs. Certain inorganic NPs may function as imaging probes, exploiting their unique magnetic or optical properties. Due to the high surface area, drug molecules can be loaded onto NPs and delivered to tumours. Employing NPs as vehicles may dramatically increase the bioavailability of drug molecules, especially those of poor solubility or stability in systemic circulation. It is possible to achieve NPs with multiple functions that can be used as a theranostic agent for simultaneous drug delivery and imaging. It is even possible to engineer NPs such that payloads can be released in response to an internal or external stimulus.[122] **Figure 18** illustrates an overview of NP

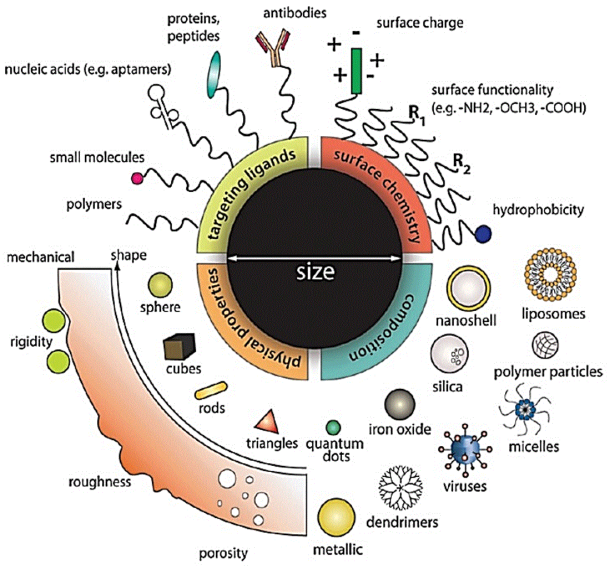

Fig. 18: Illustration demonstrating how nanomaterials can be modified for use in biomedicine. Depending on the application, various targeting ligands, surface chemistries, sizes, shapes, compositions and physical properties can be optimized to maximize the therapeutic or diagnostic ability of the material. Figure reproduced from reference 120b, Copyright 2016 MDPI.

platforms that have been investigated for use in biomedicine. For all of these applications, surface modification of monodispersed NPs is highly important for largely determining the NPs' circulation half-lives, drug loading, targeting specificity, and pharmacokinetics. Below we review some of our progress in this area, with a focus on magnetic NPs.

Surface Modification of NPs

Iron oxide NPs are by far the most studied magnetic NPs for biomedical applications.[123] In particular, iron oxide NPs have also been extensively investigated as contrast agents for magnetic resonance imaging (MRI). To take full advantage of their magnetic properties, these NPs should be monodisperse such that each individual NP has nearly identical physical and chemical properties.[124] To this end, thermal decomposition is superior to conventional co-precipitation synthesis for providing better size and crystallinity control. However, NPs made from thermal decomposition are coated with a layer of surfactants, and they cannot be dispersed in aqueous solutions. A post-synthesis surface modification is often necessary before using NPs for biomedical applications.

Catechol-based surface replacement is a common strategy for iron oxide NP modification. Catechol contains two adjacent hydroxyl groups on the phenol ring that can chelate with transition metals such as Fe with high affinity. Catechol and its analogues, for instance dopamine, can replace surface-bound oleic acid and oleylamine, and by doing so alter the surface properties of the NPs. A series of catechol analogues have been tested for this purpose.[125] For optimal colloidal stability, a hydrophilic biomolecule or polymer, such as polyethylene glycol (PEG), is often imparted along with catechol to particle surface (**Fig. 19A**). For instance, dopamine was coupled with PEG diacid of different lengths using EDC/NHS chemistry. The resulting ligands can efficiently bind to iron oxide NPs, lending them excellent colloidal stability in aqueous solutions.[126] In a separate study, dopamine was coupled with methoxy PEG using trichloro-*s*-triazine (TsT) as a crosslinker.[127] TsT is a symmetrical heterocyclic compound containing three acyl-like chlorines with varied reactivity's toward nucleophiles such as -OH or -NH_2. TsT was first coupled with $mPEG_{2000}$, and the intermediate was subsequently linked with dopamine. The resulting conjugate was also efficient at rendering iron oxide NPs soluble in water.

Macromolecules or polymers may also directly bind to particle surface. For instance, iron oxide NPs were surface-modified with dopamine, resulting in particles that can be dispersed in polar solvents such as dimethyl sulfoxide (DMSO). When adding these NPs in DMSO into human serum albumin (HSA) solutions in water, the protein molecules were adsorbed onto the particle surface, as shown in **Fig. 19B**.[128] After purification, HSA coated NPs can be collected and redispersed in buffer solutions. This method can be extended to other protein molecules, such as casein, fibrinogen, and avidin.[129] Some multidentate polymers, such as polyvinylpyrrolidone (PVP)[130] and polyaspartic acid (PASP),[131] can be added during particle synthesis, and the resulting iron oxide NPs were readily dispersed in water.

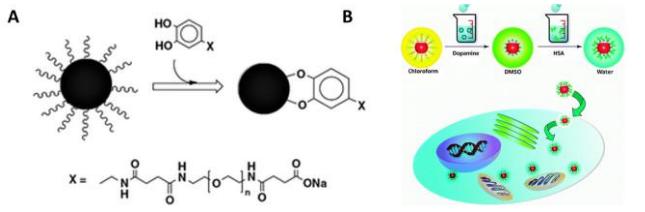

Fig. 19: Dopamine or other catechol analogues can replace surface-bound oleylamine and/or oleic acid and by doing so, alter the surface properties of iron oxide NPs. This is followed by **(A)** PEGylation and **(B)** protein adsorption to make NPs stable in aqueous solutions. Figures reproduced from refs. 124 (with permission of The Royal Society of Chemistry) and 128b (with permission of The Royal Society of Chemistry), respectively.

Surface modification not only improves NPs' colloidal stability in aqueous solutions but also reduces their chances of being opsonized and taken up by the host immune system.[132] Indeed, compared to dextran coated iron oxide NPs, those coated with PEG-dopamine showed remarkably reduced uptake by macrophages *in vitro*.[126] Such PEGylation-induced particle protection is well documented and leads to extended blood circulation of NPs.[133]

NP-based Imaging

Magnetic NPs have been extensively studied as T_2 contrast agents for MRI. For instance, Feridex, a dextran coated iron oxide formulation, has been used in the clinic for live imaging. The efficiency of T_2 reduction, measured by r_2 relaxivity, is dependent on the NP size. In general, NPs with smaller sizes have lower magnetization values and smaller r_2. Taking PVP coated iron oxide NPs for instance, when the NP size was increased from ~32 nm to ~118 nm, the r_2 relaxivity was increased from ~173 to ~249 $mM^{-1}s^{-1}$ on a 7T magnet.[130] Meanwhile, the surface coating may also have an impact on the contrast effects. For instance, when comparing Fe_5C_2 NPs coated with phospholipid, zwitterion-dopamine-sulfonate (ZDS), and casein coatings,[134] it was found that the casein coating led to an r_2 enhancement by more than 2-fold. This is attributed to the ability of casein to extend the water diffusion correlation time (τ_D), which is proportional to r_2.[135]

As afore-mentioned, NP-based tumour imaging often exploits the EPR effect.[136] Specifically, tumour blood vessels tend to feature abnormally wide gaps and abnormalities that allow for the extravasation of materials with sizes up to several hundred nanometers. This, together with the absence of effective lymphatic drainage, leads to selective accumulation of NPs in tumors.[137] For instance, when Fe_5C_2 NPs were intravenously (i.v.) injected into U87MG tumour-bearing mice, there was decent tumour accumulation at 4 h, manifested as hypointensities on T_2-weighted images.[138] This idea can be expanded to multimodality imaging probes. For example, HSA coated NPs could be labelled with both Cy5.5, a near-infrared dye molecule, and ^{64}Cu-DOTA, a radioisotope-bound chelate. The tumour accumulation of the resulting NPs was successfully monitored by three modalities: MRI, fluorescence, and PET, as shown in **Fig. 20A-C**.[128a]

To improve tumour targeting beyond the EPR effect, NPs can be coupled with a targeting ligand. For instance, c(RGDyK), a peptide with high affinity towards integrin $\alpha_v\beta_3$, was

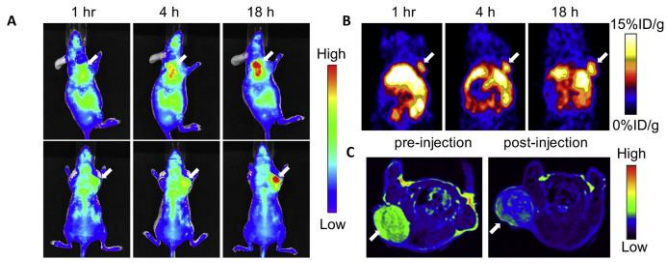

Fig. 20: Surface-modified magnetic NPs for multi-modality imaging. For instance, HSA coated iron oxide NPs can be coupled both Cy5.5 and DOTA-^{64}Cu. The resulting NPs after intravenous injection accumulated in tumors via the EPR effect. The process can be monitored by **(A)** fluorescence imaging, **(B)** PET, and **(C)** MRI. Figures are reprinted from ref. 128a with permission, Copyright 2010 Elsevier.

conjugated onto PASP coated iron oxide NPs.[131] Integrin $\alpha_v\beta_3$ is a tumour biomarker, often upregulated in tumour endothelial cells as well as many types of cancer cells.[139] When tested in U87MG tumour models, the NPs showed efficient tumour uptake that was mediated by the RGD-integrin interaction. Xie et al. synthesized ultrasmall iron oxide NPs using 4-methylcatechol (4-MC), a catechol analogue, as the surfactant. The resulting NPs could be directly coupled with c(RGDyK) through the Mannich reaction.[140] The resulting NPs showed good tumour targeting efficiency and MRI contrast when tested *in vivo*. Interestingly, unbound NPs were efficiently excreted by renal clearance due to their ultrasmall size (<10 nm in hydrodynamic diameter).

NP-based Drug Delivery

Surface-modified NPs can be loaded with therapeutics for drug delivery. For instance, Fe_3O_4 NPs were conjugated with tumstatin, a peptide with antiangiogenic and proapoptotic properties[141]. The resultant conjugate was tested in a 3D, multicellular tumour spheroid (MTS) tissue culture model,[141] which mimics the tumour environment with leaky endothelium surrounding tumour mass. This NP formulation showed selective targeting and penetration into the endothelium, and had 2 times greater uptake, and 2.7 times greater tumour neo-vascularization inhibition. Additionally, doxorubicin was loaded onto HSA coated iron oxide NPs.[142] The NPs after i.v. injection accumulated in 4T1 tumours and released doxorubicin in a sustained manner. This formulation showed a striking tumour suppression effect that was comparable to Doxil and greatly outperformed free doxorubicin.

Drug molecules can also be encapsulated within NPs that have a porous structure. One example is hollow iron oxide NPs.[143] These NPs were synthesized by the thermal decomposition of $Fe(CO)_5$, followed by oxidation with trimethylamine *N*-oxide. This initially yielded iron/iron oxide core/shell NPs, but with further oxidation, produced hollow iron oxide NPs,[143] a schematic of which is shown in **Fig. 21A**. These hollow NPs have ~2-4 nm pores on the surface through which drug molecules can enter and be encapsulated into the interior. For instance, Cheng et al. successfully loaded cisplatin into the hollow NPs.[143] The drug was released in controlled manner, with $t_{1/2}$ of 16 h. The drug loading improved the water solubility of cisplatin, and prevented premature drug degradation. In addition, they conjugated Herceptin, an anti-HER2 antibody, onto the surface of the NPs. The antibody coupling enhanced cancer cell targeting and uptake, reducing IC_{50} to 2.9 μM, which far exceeded that of free cisplatin (**Fig. 21B**).

Heterodimer NPs have also been investigated as drug delivery vehicles. Unlike single component NPs, heterodimer NPs possess two surfaces, which is advantageous if multiple functionalities are to be imparted onto particle surface. For instance, the Au-Fe_3O_4 NPs allow selective modification of Au and iron oxide surfaces by mercapto-PEG and dopamine-PEG, respectively.[144] Cisplatin could be conjugated to the Au surface, along with a HER2 antibody tethered to iron oxide for cancer cell targeting. The resulting NPs showed increased toxicity compared to free cisplatin owing to selective delivery granted by the NPs.[145]

The strong magnetism of iron oxide NPs may also permit magnet-guided drug delivery.[146] For example, iron oxide NPs were loaded onto diatom shells and the resulting particles were investigated as a potential drug delivery vehicle. Diatoms are a major group of algae that are encased within a silica shell called a frustule. These diatom shells have a length of ~10 μm with ~500 nm pores on their surface. This unique feature allows them to encapsulate hundreds of magnetic NPs, and in doing so, grants the diatom with a superior magnetic response. In a proof-of-concept study, dye molecules as drug mimics were encapsulated along with iron oxide NPs into diatoms.[146] These diatoms were i.v. injected into mice bearing subcutaneously

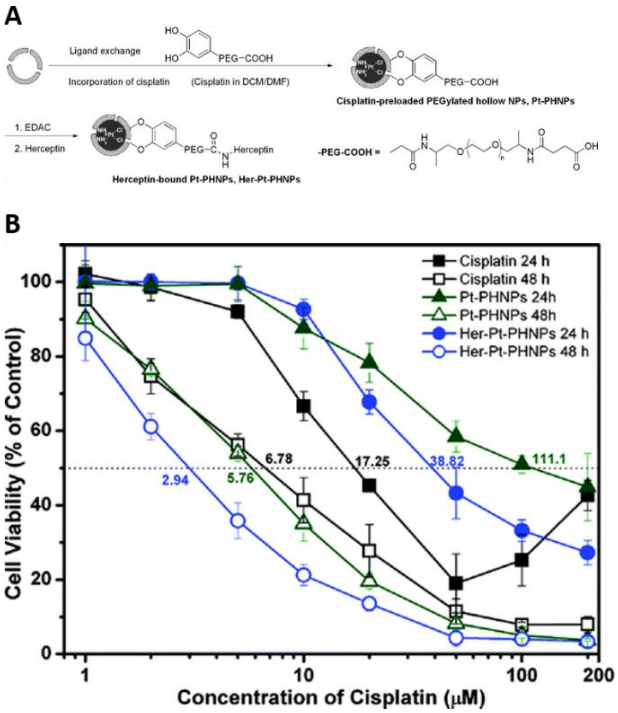

Fig. 21: Surface modified magnetic NPs for drug delivery. **(A)** Cisplatin can be encapsulated into the interior of hollow iron oxide NPs. The particle surface can be modified with PEGylated dopamine and then coupled with Herceptin for cancer cell targeting, **(B)** cytotoxicity studies. Compared with free cisplatin, cisplatin NPs led to much more efficient cancer cell killing. Figures are reprinted from ref. 143 with permission, Copyright 2009 American Chemical Society.

inoculated tumours. Using fluorescence imaging and MRI, it was confirmed that enhanced tumour accumulation was achieved when an external magnetic field was applied to tumour areas.

Conclusions and Future Outlook

Advances in monodisperse NP synthesis and characterization have allowed nearly every application of NPs to flourish. In this review, we have discussed the syntheses of monodisperse NPs and their selected applications in catalysis and nanomedicine, both of which are of paramount importance to decipher any structure-property relationships of the NPs. We summarize recent advances of solution phase chemical synthesis of monodisperse NPs. Most of the syntheses follow the classical La Mer model on growing colloidal particles and require generally nucleation and growth stages for the formation of NPs to a desired size that should be further capped with surfactant(s) for NP stabilization in the reaction solution. The versatile solution phase chemistry allows fine-tuning of reaction parameters, leading to the formation of monodisperse NPs. Depending on synthetic condition applied in the synthesis, the growth can yield thermodynamically stable polyhedral NPs, or kinetically-controlled NPs with a designated shape. With controlled nucleation, the synthesis can be extended to grow shells on the seeding NPs (seed-mediated growth), making it possible to control not only NP sizes, but also heterostructured multicomponent systems for the formation of core/shell and dumbbell-like composite NPs.

These size, shape and complexity controls realized in the synthesis yield NPs with more precise surface chemistry and physical properties that are important for the next step: applications. For example, the NP catalysis can now be tuned and optimized for oxygen reduction reaction, CO_2 reduction and cascade dehydrogenation/hydrogenations to functional organic compounds in greener chemistry synthesis conditions. NPs with tunable physical properties and controlled surface chemistry are also explored extensively for understanding NP chemistry in biological systems to achieve the desired NP biocompatibility, biocirculation, biodistribution, and bioelimination. In this review, we focus on highlighting monodisperse iron oxide NPs and their controlled surface functionalization for target-specific cancer imaging and anti-cancer drug delivery. These studies have demonstrated that monodisperse NPs have risen as the ideal model systems to determine how small changes on the nanoscale can affect NP properties and NP interactions with biology.

Despite the advances made in the synthesis and extensive studies devoted to monodisperse NPs, more challenges still exist and overcoming these challenges is essential for NPs to demonstrate practical uses. On synthetic side, using solution phase synthesis is still difficult to produce monodisperse NPs at commercial scale. Those prepared and sold commercially tend to be less monodisperse than those demonstrated from lab scale synthesis. NPs do have intrinsic large surface energy, which often facilitates their binding nonselectively with any molecules present adjacent to them, making it very difficult to control/quantify NP surface chemistry. NPs with energetically unfavorable shapes or morphologies may not be stable, and as a result, the low-coordination atoms on the NP surface have high chemical potentials and tend to relax to find the low energy spots, degrading the shape quality and properties of the NPs. Robust coatings are generally needed, which unfortunately often compromise the NP surface chemistry. In catalysis, it is extremely important to have a stable NP surface where a chemical reaction can be monitored and a catalytic pathway can be elucidated. However, the dynamic nature of the NP surface in the catalytic reaction conditions, especially in high temperature and corrosive conditions, makes it difficult to stabilize NPs for reaction observation/characterization. NP interactions with biomolecules are key for the NPs to be applicable to the proposed biomedicine uses to achieve sensitive biomedical imaging and efficient therapy, which relies essentially on developing NPs with predictable surface chemistry and biological interactions.

The encouraging news is that decades of efforts on NP studies have yielded methodologies that allow us to achieve unprecedented control on NP dimensions and properties. These pave the way for further studies on understanding NP stability, surface chemistry, surface reactivity, and bioconjugation. Monodisperse NPs will be utilized as successful model systems for understanding structure-property relationships and as practical catalysts or probes for advanced nanotechnological applications.

Conflicts of interest

There are no conflicts to declare.

Acknowledgements

Work at Brown University was supported by the US Department of Energy, Fuel Cell Technologies Office, the American Chemical Society Petroleum Research Fund (57114-ND5), the Office of Vice President of Research of Brown University, the Institute of Molecular and Nanoscale Innovation of Brown University, and Strem Chemicals, as well as in part by the U.S. Army Research Laboratory and the U.S. Army Research Office under the Multi University Research Initiative MURI (W911NF-11-1-0353) on "Stress-Controlled Catalysis via Engineered Nanostructures," the U.S. Army Research Laboratory and the U.S. Army Research Office under grant W911NF-15-1-0147, the Center for the Capture and Conversion of CO_2, a Center for Chemical Innovation funded by the National Science Foundation, CHE-1240020. M. M. is supported by the National Science Foundation Graduate Research Fellowship, under Grant No. 1644760. Work at the University of Georgia was supported by the National Science Foundation (CAREER grant no. NSF1552617) and the National Institute of Biomedical Imaging and Bioengineering (grant no. R01EB022596).

References

1 (a) C. B. Murray, C. R. Kagan and M. G. Bawendi, *Annu. Rev. Mater. Sci.*, 2000, **30**, 545–610.; (b) L. Wu, A. Mendoza-Garcia, Q. Li and S. Sun, *Chem. Rev.,* 2016, **116**, 10473-10512.; (c) Y.

Yin and D. Talapin, *Chem. Soc. Rev.*, 2013, **42**, 2484–2487.; (d) M. V. Kovalenko, L. Manna, A. Cabot, Z. Hens, D. V. Talapin, C. R. Kagan, V. I. Klimov, A. L. Rogach, P. Reiss, D. J. Milliron, P. Guyot-Sionnnest, G. Konstantatos, W. J. Parak, T. Hyeon, B. A. Korgel, C. B. Murray and W. Heiss, *ACS Nano*, 2015, **9**, 1012–1057.

2 F. J. Heiligtag and M. Niederberger, *Mater. Today*, 2013, **16**, 262–271

3 S. Sun, *Adv. Mater.*, 2006, **18**, 393–403.

4 (a) E. Roduner, *Chem. Soc. Rev.*, 2006, **35**, 583–593.; (b) S. Eustis and M. A. El-Sayed, *Chem. Soc. Rev.*, 2006, **35,** 209–217.

5 (a) Q. L. Zhu and Q. Xu, *Chem*, 2016, 220–245.; (b) M. Cargnello, V. V. T. Doan-Nguyen, T. R. Gordon, R. E. Diaz, E. A. Stach, R. J. Gorte, P. Fornasiero and C. B. Murray, *Science*, 2013, **341**, 771–773.; (c) P. Losch, W. Huang, E. D. Goodman, C. J. Wrasman, A. Holm, A. R. Riscoe, J. A. Schwalbe and M. Cargnello, *Nano Today*, 2019, **24,** 15–47.

6 (a) N. A. Frey, S. Peng, K. Cheng and S. Sun, *Chem. Soc. Rev.*, 2009, **38,** 2532–2542.; (b) D. K. Yi, S. T. Selvan, S. S. Lee, G. C. Papaefthymiou, D. Kundaliya and J. Y. Ying, *J. Am. Chem. Soc.*, 2005, **127**, 4990–4991.; (c) D. V. Talapin, J. S. Lee, M. V. Kovalenko and E. V. Shevchenko, *Chem. Rev.*, 2010, **110**, 389–458.; (d) X. Peng, L. Manna, W. Yang, J. Wickham, E. Scher, A. Kadavanich and A. P. Alivisatos, *Nature*, 2000, **404**, 59–61.

7 (a) O. Chen, J. Zhao, V. P. Chauhan, J. Cui, C. Wong, D. K. Harris, H. Wei, H. S. Han, D. Fukumura, R. K. Jain and M. G. Bawendi, *Nat. Mater.*, 2013, **12**, 445–451.; (b) H. S. Mansur, *Wiley Interdiscip. Rev.: Nanomed. Nanobiotechnol.*, 2010, **2**, 113–129.

8 (a) D. L. Leslie-Pelecky and R. D. Rieke, *Chem. Mater.*, 1996, **8**, 1770–1783.; (b) B. H. Kim, N. Lee, H. Kim, K. An, Y. Il Park, Y. Choi, K. Shin, Y. Lee, S. G. Kwon, H. Bin Na, J. G. Park, T. Y. Ahn, Y. W. Kim, W. K. Moon, S. H. Choi and T. Hyeon, *J. Am. Chem. Soc.*, 2011, **133**, 12624–12631.; (c) L. Wu, Q. Li, C. H. Wu, H. Zhu, A. Mendoza-Garcia, B. Shen, J. Guo and S. Sun, *J. Am. Chem. Soc.*, 2015, **137**, 7071–7074.

9 (a) Y. W. Jun, J. S. Choi and J. Cheon, *Angew. Chemie - Int. Ed.*, 2006, **45**, 3414-3439.; (b) J. Park, J. Joo, G. K. Soon, Y. Jang and T. Hyeon, *Angew. Chemie - Int. Ed.*, 2007, **46**, 4630–4660.

10 (a) A. R. Tao, S. Habas and P. Yang, *Small*, 2008, 310–325.; (b) K. An and G. A. Somorjai, *ChemCatChem*, 2012, 1512–1524.

11 N. T. K. Thanh, N. Maclean and S. Mahiddine, *Chem. Rev.*, 2014, 7610–7630.

12 Y. Xia, Y. Xiong, B. Lim and S. E. Skrabalak, *Angew. Chemie - Int. Ed.*, 2009, 60–103.

13 (a) H. Hiramatsu and F. E. Osterloh, *Chem. Mater.*, 2004, **16**, 2509–2511.; (b) S. Peng, Y. Lee, C. Wang, H. Yin, S. Dai and S. Sun, *Nano Res.*, 2008, **1**, 229–234.; (c) C. Shen, C. Hui, T. Yang, C. Xiao, J. Tian, L. Bao, S. Chen, H. Ding and H. Gao, *Chem. Mater.*, 2008, **20**, 6939–6944.

14 S. Guo, S. Zhang, L. Wu and S. Sun, *Angew. Chemie - Int. Ed.*, 2012, **51**, 11770–11773.

15 S. Peng, C. Wang, J. Xie and S. Sun, *J. Am. Chem. Soc.*, 2006, **128**, 10676–10677.

16 J. Park, K. An, Y. Hwang, J. E. G. Park, H. J. Noh, J. Y. Kim, J. H. Park, N. M. Hwang and T. Hyeon, *Nat. Mater.*, 2004, **3**, 891–895.

17 (a) S. Sun, C. B. Murray, D. Weller, L. Folks and A. Moser, *Science*, 2000, **287**, 1989–1992.; (b) M. Chen, J. P. Liu and S. Sun, *J. Am. Chem. Soc.*, 2004, **126**, 8394–8395.

18 (a) H. Göksu, S. F. Ho, Ö. Metin, K. Korkmaz, A. Mendoza Garcia, M. S. Gültekin and S. Sun, *ACS Catal.*, 2014, **4**, 1777–1782.; (b) C. Yu, X. Guo, M. Shen, B. Shen, M. Muzzio, Z. Yin, Q. Li, Z. Xi, J. Li, C. T. Seto and S. Sun, *Angew. Chemie - Int. Ed.*, 2018, **57**, 451–455.

19 (a) C. Wang, H. Yin, R. Chan, S. Peng, S. Dai and S. Sun, *Chem. Mater.*, 2009, **21**, 433–435.; (b) S. F. Ho, A. Mendoza-Garcia, S. Guo, K. He, D. Su, S. Liu, Ö. Metin and S. Sun, *Nanoscale*, 2014, **6**, 6970–6973.; (c) M. Muzzio, C. Yu, H. Lin, T. Yom, D. A. Boga, Z. Xi, N. Li, Z. Yin, J. Li, J. A. Dunn and S. Sun, *Green Chem.*, 2019, **21**, 1895–1899.; (d) Y. Liu, D. Li, V. R. Stamenkovic, S. Soled, J. D. Henao and S. Sun, *ACS Catal.*, 2011, **1**, 1719–1723.; (e) S. Zhou, H. Yin, V. Schwartz, Z. Wu, D. Mullins, B. Eichhorn, S. H. Overbury and S. Dai, *ChemPhysChem*, 2008, **9**, 2475–2479.; (f) C. H. Wu, C. Liu, D. Su, H. L. Xin, H. T. Fang, B. Eren, S. Zhang, C. B. Murray and M. B. Salmeron, *Nat. Catal.*, 2019, **2**, 78–85.

20 G. Lee, J. H. Shim, H. Kang, K. M. Nam, H. Song and J. T. Park, *Chem. Commun.*, 2009, 5036–5038.

21 (a) C. Wang, H. Daimon, Y. Lee, J. Kim and S. Sun, *J. Am. Chem. Soc.*, 2007, **129**, 6974–6975.; (b) Y. Kang, X. Ye and C. B. Murray, *Angew. Chemie - Int. Ed.*, 2010, **49**, 6156–6159.

22 (a) S. I. Lim, I. Ojea-Jiménez, M. Varon, E. Casals, J. Arbiol and V. Puntes, Nano Lett., 2010, **10**, 964–973.; (b) Y. Kang, J. B. Pyo, X. Ye, R. E. Diaz, T. R. Gordon, E. A. Stach and C. B. Murray, *ACS Nano*, 2013, **7**, 645–653.; (c) J. Wu, A. Gross and H. Yang, *Nano Lett.*, 2011, **11**, 798–802.

23 (a) S. Zhou, J. Li, K. D. Gilroy, J. Tao, C. Zhu, X. Yang, X. Sun and Y. Xia, *ACS Nano*, 2016, **10**, 9861–9870.; (b) X. Xia, J. Zhang, N. Lu, M. J. Kim, K. Ghale, Y. Xu, E. McKenzie, J. Liu and H. Ye, *ACS Nano*, 2015, **9**, 9994–10004.

24 (a) Q. Zhang, L. Han, H. Jing, D. A. Blom, Y. Lin, H. L. Xin and H. Wang, *ACS Nano*, 2016, **10**, 2960–2974.; (b) H. H. Chang and C. J. Murphy, *Chem. Mater.*, 2018, **30**, 1427–1435.

25 X. Ye, L. Jin, H. Caglayan, J. Chen, G. Xing, C. Zheng, V. Doan-Nguyen, Y. Kang, N. Engheta, C. R. Kagan and C. B. Murray, *ACS Nano*, 2012, **6**, 2804–2817.

26 C. J. Desantis, A. A. Peverly, D. G. Peters and S. E. Skrabalak, *Nano Lett.*, 2011, **11**, 2164–2168.

27 L. Wu, P. O. Jubert, D. Berman, W. Imaino, A. Nelson, H. Zhu, S. Zhang and S. Sun, *Nano Lett.*, 2014, **14**, 3395–3399.

28 (a) S. B. Wang, Y. L. Min and S. H. Yu, *J. Phys. Chem. C*, 2007, **111**, 3551–3554.; (b) S. Guo, S. Zhang, D. Su and S. Sun, *J. Am. Chem. Soc.*, 2013, **135**, 13879–13884.

29 (a) C. Wang, Y. Hou, J. Kim and S. Sun, *Angew. Chemie - Int. Ed.*, 2007, **46**, 6333–6335.; (b) S. Guo, D. Li, H. Zhu, S. Zhang, N. M. Markovic, V. R. Stamenkovic and S. Sun, *Angew. Chemie - Int. Ed.*, 2013, **52**, 3465–3468.

30 (a) A. Gole and C. J. Murphy, *Chem. Mater.*, 2004, **16**, 3633–3640.; (b) S. Sun and H. Zeng, *J. Am. Chem. Soc.*, 2002, **124**, 8204–8205.

31 V. Mazumder, M. Chi, K. L. More and S. Sun, *Angew. Chemie - Int. Ed.*, 2010, **49**, 9368–9372.

32 A. M. Henning, J. Watt, P. J. Miedziak, S. Cheong, M. Santonastaso, M. Song, Y. Takeda, A. I. Kirkland, S. H. Taylor and R. D. Tilley, *Angew. Chemie - Int. Ed.*, 2013, **52**, 1477–1480.

33 (a) H. Zeng, J. Li, Z. L. Wang, J. P. Liu and S. Sun, *Nano Lett.*, 2004, **4**, 187–190.; (b) Q. Li, J. Fu, W. Zhu, Z. Chen, B. Shen, L. Wu, Z. Xi, T. Wang, G. Lu, J. J. Zhu and S. Sun, *J. Am. Chem. Soc.*, 2017, **139**, 4290–4293.; (c) Z. Xu, Y. Hou and S. Sun, *J. Am. Chem. Soc.*, 2007, **129**, 8698–8699.; (d) M. B. Gawande, A. Goswami, T. Asefa, H. Guo, A. V. Biradar, D. L. Peng, R. Zboril and R. S. Varma, *Chem. Soc. Rev.*, 2015, **44,** 7540–7590.; (e) L. Arroyo-Ramírez, C. Chen, M. Cargnello, C. B. Murray, P. Fornasiero and R. J. Gorte, *J. Mater. Chem. A*, 2014, **2**, 19509–19514.

34 S. Zhang, Y. Hao, D. Su, V. V. T. Doan-Nguyen, Y. Wu, J. Li, S. Sun and C. B. Murray, *J. Am. Chem. Soc.*, 2014, **136**, 15921–15924.

35 P. C. Chen, M. Liu, J. S. Du, B. Meckes, S. Wang, H. Lin, V. P. Dravid, C. Wolverton and C. A. Mirkin, *Science*, 2019, **363**, 959–964.

36 C. Wang, H. Yin, S. Dai and S. Sun, *Chem. Mater.*, 2010, **22**, 3277–3282.

37 (a) W. Yang, W. Lei, Y. Yu, W. Zhu, T. A. George, X. Z. Li, D. J. Sellmyer and S. Sun, *J. Mater. Chem. C*, 2015, **3**, 7075–7080.; (b) W. Yang, Y. Yu, Y. Tang, K. Li, Z. Zhao, M. Li, G. Yin, H. Li and S. Sun, *Nanoscale*, 2017, **9**, 1022–1027.
38 J. Lai, B. Huang, Y. Tang, F. Lin, P. Zhou, X. Chen, Y. Sun, F. Lv and S. Guo, *Chem*, 2018, **4**, 1153–1166.
39 R. Scarfiello, C. Nobile and P. D. Cozzoli, *Front. Mater.*, 2016, DOI:10.3389/fmats.2016.00056.
40 H. Wu, O. Chen, J. Zhuang, J. Lynch, D. Lamontagne, Y. Nagaoka and Y. C. Cao, *J. Am. Chem. Soc.*, 2011, **133**, 14327–14337.
41 (a) C. Wang, H. Yin, S. Dai and S. Sun, *Chem. Mater.*, 2010, **22**, 3277–3282.; (a) R. W. Lord, C. F. Holder, J. L. Fenton and R. E. Schaak, *Chem. Mater.*, 2019, **31**, 4605–4613.
42 M. R. Buck, J. F. Bondi and R. E. Schaak, *Nat. Chem.*, 2012, **4**, 37–44.
43 (a) J. L. Fenton, B. C. Steimle and R. E. Schaak, *Inorg. Chem.*, 2019, **58**, 672–678.; (b) J. L. Fenton, B. C. Steimle and R. E. Schaak, *Science.*, 2018, **360**, 513–517.; (c) Y. Liu, M. Liu, D. Yin, L. Qiao, Z. Fu and M. T. Swihart, *ACS Nano*, 2018, **12**, 7803–7811. (c) B. D. Anderson and J. B. Tracy, *Nanoscale*, 2014, **6,** 12195–12216.; (d) 1 J. Lee, J. Yang, S. G. Kwon and T. Hyeon, *Nat. Rev. Mater.*, 2016, **1,** 16034.
44 (a) X. Yu, A. Shavel, X. An, Z. Luo, M. Ibáñez and A. Cabot, *J. Am. Chem. Soc.*, 2014, **136**, 9236–9239.; (b) S. K. Balakrishnan and P. V. Kamat, *ACS Energy Lett.*, 2017, **2**, 88–93.; (c) L. Amirav, F. Oba, S. Aloni and A. P. Alivisatos, *Angew. Chemie Int. Ed.*, 2015, **54**, 7007–7011.
45 H. Zhu, Z. Fan, L. Yu, M. A. Wilson, Y. Nagaoka, D. Eggert, C. Cao, Y. Liu, Z. Wei, X. Wang, J. He, J. Zhao, R. Li, Z. Wang, M. Grünwald and O. Chen, *J. Am. Chem. Soc.*, 2019, **141**, 6013–6021.
46 (a) S. Chu and A. Majumdar, *Nature*, 2012, **488**, 294-303.; (b) Z. W. Seh, J. Kibsgaard, C. F. Dickens, I. Chorkendorff, J. K. Nørskov and T. F. Jaramillo, *Science*, 2017, **355**, eaad4998.
47 (a) C. C. L. McCrory, S. Jung, J. C. Peters and T. F. Jaramillo, *J. Am. Chem. Soc.*, 2013, **135**, 16977–16987.; (b) C. Wang, J. Jiang, T. Ding, G. Chen, W. Xu and Q. Yang, *Adv. Mater. Interfaces*, 2016, **3**, 1500454**.**
48 (a) F. Yang, Y. Zhao, Y. Du, Y. Chen, G. Cheng, S. Chen and W. Luo, *Adv. Energy Mater.*, 2018, **8**.; (b) H. Lv, Z. Xi, Z. Chen, S. Guo, Y. Yu, W. Zhu, Q. Li, X. Zhang, M. Pan, G. Lu, S. Mu and S. Sun, *J. Am. Chem. Soc.*, 2015, **137**, 5859–5862.
49 (a) Y. Liu, M. Wei, D. Raciti, Y. Wang, P. Hu, J. H. Park, M. Barclay and C. Wang, *ACS Catal.*, 2018, **8**, 10931–10937.; (b) J. Li, S. Z. Jilani, H. Lin, X. Liu, K. Wei, Y. Jia, P. Zhang, M. Chi, Y. J. Tong, Z. Xi and S. Sun, *Angew. Chemie Int. Ed.*, DOI:10.1002/anie.201906137.
50 Z. Lu, G. Chen, S. Siahrostami, Z. Chen, K. Liu, J. Xie, L. Liao, T. Wu, Di. Lin, Y. Liu, T. F. Jaramillo, J. K. Nørskov and Y. Cui, *Nat. Catal.*, 2018, **1**, 156–162.
51 S. Z. Andersen, V. Čolić, S. Yang, J. A. Schwalbe, A. C. Nielander, J. M. McEnaney, K. Enemark-Rasmussen, J. G. Baker, A. R. Singh, B. A. Rohr, M. J. Statt, S. J. Blair, S. Mezzavilla, J. Kibsgaard, P. C. K. Vesborg, M. Cargnello, S. F. Bent, T. F. Jaramillo, I. E. L. Stephens, J. K. Nørskov and I. Chorkendorff, *Nature*, 2019, **570**, 504–508.
52 (a) E. Roduner, *Chem. Soc. Rev.*, 2014, 8226–8239.; (b) M. A. Ardagh, O. Abdelrahman and P. J. Dauenhauer, *ACS Catal.*, 2019, **8**, 6929–6937.
53 B. Hinnemann, P. G. Moses, J. Bonde, K. P. Jørgensen, J. H. Nielsen, S. Horch, I. Chorkendorff and J. K. Nørskov, *J. Am. Chem. Soc.*, 2005, **127**, 5308-5309.
54 E. Skúlason, V. Tripkovic, M. E. Björketun, S. Gudmundsdottir, G. Karlberg, J. Rossmeisl, T. Bligaard, H. Jónsson and J. K. Nørskov, *J. Phys. Chem. C*, 2010, **114**, 18182-18197.
55 W. Sheng, H. A. Gasteiger and Y. Shao-Horn, *Journal of The Electrochemical Society*, 2010, **157**, B1529-B1536.
56 (a) A. Khorshidi, J. Violet, J. Hashemi and A. A. Peterson, *Nat. Catal.*, 2018, **1**, 263.; (b) A. Vojvodic and J. K. Nørskov, *National Science Review*, 2015, **2**, 140-143.
57 P. Wang, F. Chang, W. Gao, J. Guo, G. Wu, T. He and P. Chen, *Nat. Chem.*, 2017, **9**, 64.
58 (a) G. Kumar, E. Nikolla, S. Linic, J. W. Medlin and M. J. Janik, *ACS Catalysis*, 2018, **8**, 3202-3208.; (b) K. D. Gilroy, X. Yang, S. Xie, M. Zhao, D. Qin and Y. Xia, *Advanced Materials*, 2018, **30**, 1706312.; (c) K. D. Gilroy, A. Ruditskiy, H.-C. Peng, D. Qin and Y. Xia, *Chem. Rev.*, 2016, **116**, 10414-10472.
59 X. X. Wang, M. T. Swihart and G. Wu, *Nat. Catal.*, 2019, **2**, 578–589.
60 J. K. Nørskov, J. Rossmeisl, A. Logadottir, L. Lindqvist, J. R. Kitchin, T. Bligaard and H. Jonsson, *The Journal of Physical Chemistry B*, 2004, **108**, 17886-17892.
61 W. Sheng, S. Chen, E. Vescovo and Y. Shao-Horn, *J. Electrochem. Soc.*, 2011, **166**, B96–B103.
62 V. R. Stamenkovic, B. Fowler, B. S. Mun, G. Wang, P. N. Ross, C. A. Lucas and N. M. Markovic, *Science*, 2007, **315**, 493–497.
63 N. Markovic, H. Gasteiger and P. N. Ross, *Journal of the Electrochemical Society*, 1997, **144**, 1591-1597.
64 (a) M. Luo and S. Guo, *Nature Reviews Materials*, 2017, **2**, 17059.; (b) I. E. L. Stephens, J. Rossmeisl and I. Chorkendorff, *Science*, 2016, **354**, 1378-1379.; (c) W. Xia, A. Mahmood, Z. Liang, R. Zou and S. Guo, *Angew. Chemie - Int. Ed.,* 2016, **55**, 2650-2676.
65 (a) C. Cui, L. Gan, M. Heggen, S. Rudi and P. Strasser, *Nat. Mat.*, 2013, **12**, 765.; (b) S.-I. Choi, S. Xie, M. Shao, J. H. Odell, N. Lu, H.-C. Peng, L. Protsailo, S. Guerrero, J. Park and X. Xia, *Nano Lett.*, 2013, **13**, 3420-3425.
66 X. Huang, Z. Zhao, L. Cao, Y. Chen, E. Zhu, Z. Lin, M. Li, A. Yan, A. Zettl, Y. M. Wang, X. Duan, T. Mueller, and Y. Huang, *Science*, 2015, **348**, 1230-1234.
67 C. Chen, Y. Kang, Z. Huo, Z. Zhu, W. Huang, H. L. Xin, J. D. Snyder, D. Li, J. A. Herron, M. Mavrikakis, M. Chi, K. L. More, Y. Li, N. M. Markovic, G. A. Somorjai, P. Yang, and V. R. Stamenkovic, *Science*, 2014, **343**, 1339-1343.
68 M. Li, Z. Zhao, T. Cheng, A. Fortunelli, C. Y. Chen, R. Yu, Q. Zhang, L. Gu, B. V. Merinov, Z. Lin, E. Zhu, T. Yu, Q. Jia, J. Guo, L. Zhang, W. A. Goddard, Y. Huang and X. Duan, *Science*, 2016, **354**, 1414–1419.
69 B. Han, C. E. Carlton, A. Kongkanand, R. S. Kukreja, B. R. Theobald, L. Gan, R. O'Malley, P. Strasser, F. T. Wagner and Y. Shao-Horn, *Energy & Environmental Science*, 2015, **8**, 258-266
70 (a) Q. Li, L. Wu, G. Wu, D. Su, H. Lv, S. Zhang, W. Zhu, A. Casimir, H. Zhu, A. Mendoza-Garcia and S. Sun, *Nano Lett.*, 2015, 2468–2473.; (b) J. Kim, Y. Lee and S. Sun, *J. Am. Chem. Soc.*, 2010, **132**, 4996–4997.; (c) C. Wang, X. Sang, J. T. L. Gamler, D. P. Chen, R. R. Unocic and S. E. Skrabalak, *Nano Lett.*, 2017, **17**, 5526–5532.
71 J. Li, S. Sharma, X. Liu, Y. T. Pan, J. S. Spendelow, M. Chi, Y. Jia, P. Zhang, D. A. Cullen, Z. Xi, H. Lin, Z. Yin, B. Shen, M. Muzzio, C. Yu, Y. S. Kim, A. A. Peterson, K. L. More, H. Zhu and S. Sun, *Joule*, 2019, **3**, 124–135.
72 J. Li, Z. Xi, Y. T. Pan, J. S. Spendelow, P. N. Duchesne, D. Su, Q. Li, C. Yu, Z. Yin, B. Shen, Y. S. Kim, P. Zhang and S. Sun, *J. Am. Chem. Soc.*, 2018, **140**, 2926–2932.
73 L. Bu, N. Zhang, S. Guo, X. Zhang, J. Li, J. Yao, T. Wu, G. Lu, J.-Y. Ma, D. Su, and X. Huang, *Science*, 2016, **354**, 1410-1414.
74 L. Chong, J. Wen, J. Kubal, F. G. Sen, J. Zou, J. Greeley, M. Chan, H. Barkholtz, W. Ding and D.-J. Liu, *Science*, 2018, **362**, 1276-1281.
75 (a) G. Wu, K. L. More, C. M. Johnston and P. Zelenay, *Science*, 2011, **332**, 443-447.; (b) G. Wu and P. Zelenay, *Acc. Chem. Res.*, 2013, **46**, 1878-1889.
76 Y. Hori, K. Kikuchi and S. Suzuki, *Chem. Lett.,* 1985, **14**, 1695-1698.

77 (a) W. Zhang, Y. Hu, L. Ma, G. Zhu, Y. Wang, X. Xue, R. Chen, S. Yang and Z. Jin, *Adv. Sci.*, 2018, **5**.; (b) O. S. Bushuyev, P. De Luna, C. T. Dinh, L. Tao, G. Saur, J. van de Lagemaat, S. O. Kelley and E. H. Sargent, *Joule*, 2018, 825–832.

78 (a) C. W. Li and M. W. Kanan, *J. Am. Chem. Soc.*, 2012, **134**, 7231–7231.; (b) X. Feng, K. Jiang, S. Fan and M. W. Kanan, *J. Am. Chem. Soc.*, 2015, **137**, 4606–4609.

79 Y. Chen, C. W. Li and M. W. Kanan, *J. Am. Chem. Soc.*, 2012, **134**, 19969–19972.;

80 W. Zhu, R. Michalsky, Ö. Metin, H. Lv, S. Guo, C. J. Wright, X. Sun, A. A. Peterson and S. Sun, *J. Am. Chem. Soc.*, 2013, **135**, 16833–16836.

81 W. Zhu, Y. J. Zhang, H. Zhang, H. Lv, Q. Li, R. Michalsky, A. A. Peterson and S. Sun, *J. Am. Chem. Soc.*, 2014, **136**, 16132–16135.

82 (a) Z. Zhang, M. Chi, G. M. Veith, P. Zhang, D. A. Lutterman, J. Rosenthal, S. H. Overbury, S. Dai and H. Zhu, *ACS Catal.*, 2016, **6**, 6255–6264.; (b) D. Gao, H. Zhou, J. Wang, S. Miao, F. Yang, G. Wang, J. Wang and X. Bao, *J. Am. Chem. Soc.*, 2015, **137**, 4288–4291.; (c) C. Kim, H. S. Jeon, T. Eom, M. S. Jee, H. Kim, C. M. Friend, B. K. Min and Y. J. Hwang, *J. Am. Chem. Soc.*, 2015, **137**, 13844–13850.

83 H. Xie, S. Chen, F. Ma, J. Liang, Z. Miao, T. Wang, H. L. Wang, Y. Huang and Q. Li, *ACS Appl. Mater. Interfaces*, 2018, **10**, 36996–37004.

84 W. Luc, C. Collins, S. Wang, H. Xin, K. He, Y. Kang and F. Jiao, *J. Am. Chem. Soc.*, 2017, **139**, 1885–1893.

85 (a) Y. Lum and J. W. Ager, *Angew. Chemie - Int. Ed.*, 2018, **57**, 551–554.; (b) S. Nitopi, E. Bertheussen, S. B. Scott, X. Liu, A. K. Engstfeld, S. Horch, B. Seger, I. E. L. Stephens, K. Chan, C. Hahn, J. K. Nørskov, T. F. Jaramillo and I. Chorkendorff, *Chem. Rev.*, 2019, **119**, 7610–7672.

86 D. Kim, J. Resasco, Y. Yu, A. M. Asiri and P. Yang, *Nat. Commun.*, 2014, **5**, 4948.

87 Y. Mun, S. Lee, A. Cho, S. Kim, J. W. Han and J. Lee, *Appl. Catal. B Environ.*, 2019, **246**, 82–88.

88 Q. Li, W. Zhu, J. Fu, H. Zhang, G. Wu and S. Sun, *Nano Energy*, 2016, **24**, 1–9.

89 (a) Y. Li, F. Cui, M. B. Ross, D. Kim, Y. Sun and P. Yang, *Nano Lett.*, 2017, **17**, 1312–1317.; (b) H. Zhang, Y. Zhang, Y. Li, S. Ahn, G. T. R. Palmore, J. Fu, A. A. Peterson and S. Sun, *Nanoscale*, 2019, **11**, 12075–12079.;s (c) D. Raciti, K. J. Livi and C. Wang, *Nano Lett.*, 2015, **15**, 6829–6835.

90 (a) G. Gurudayal, D. Perone, S. Malani, Y. Lum, S. Haussener and J. W. Ager, *ACS Appl. Energy Mater.*, 2019, **2**, 4551–4559. (b) J. Gao, D. Ren, X. Guo, S. M. Zakeeruddin and M. Grätzel, *Faraday Discuss.*, 2019, **215**, 282–296. (c) J. Fu, W. Zhu, Y. Chen, Z. Yin, Y. Li, J. Liu, H. Zhang, J.-J. Zhu, S. Sun, *Angew. Chem. Int. Ed*. **2019**, 10.1002/anie.201905318.

91 P. Anastas and N. Eghbali, *Chem. Soc. Rev.,* 2010, **39**, 301–312.

92 (a) R. A. Sheldon and R. S. Downing, *Appl. Catal. A Gen.*, 1999, **189**, 163–183.; (b) D. Astruc, F. Lu and J. R. Aranzaes, *Angew. Chemie - Int. Ed.*, 2005, **44**, 7852–7872.; (c) L. M. Rossi, N. J. S. Costa, F. P. Silva and R. Wojcieszak, *Green Chem.*, 2014, **16**, 2906–2933.

93 (a) T. B. Marder, *Angew. Chemie - Int. Ed.*, 2007, **46**, 8116–8118.; (b) U. Sanyal, U. B. Demirci, B. R. Jagirdar and P. Miele, *ChemSusChem*, 2011, **4**, 1731–1739.

94 A. Staubitz, A. P. M. Robertson and I. Manners, *Chem. Rev.*, 2010, **110**, 4079–4124.

95 (a) Y. Chen, X. Yang, M. Kitta and Q. Xu, *Nano Res.*, 2017, **10**, 3811–3816.; (b) B. Kiliç, S. Şencanli and Ö. Metin, *J. Mol. Catal. A Chem.*, 2012, **361**–**362**, 104–110.; (c) H. Can and Ö. Metin, *Appl. Catal. B Environ.*, 2012, **125**, 304–310.; (d) Ö. Metin, V. Mazumder, S. Özkar and S. Sun, *J. Am. Chem. Soc.*, 2010, **132**, 1468–1469.; (e) Q. Yao, Z. H. Lu, Z. Zhang, X. Chen and Y. Lan, *Sci. Rep.*, 2014, **4**, 7597.; (f) K. Guo, H. Li and Z. Yu, *ACS Appl. Mater. Interfaces*, 2018, **10**, 517–525.; (g) H. Ma and C. Na, *ACS Catal.*, 2015, **5**, 1726–1735.; (h) L. Cui, X. Cao, X. Sun, W. Yang and J. Liu, *ChemCatChem*, 2018, **10**, 710–715.

96 W. W. Zhan, Q. L. Zhu and Q. Xu, *ACS Catal.*, 2016, **6**, 6892–6905.

97 (a) D. Sun, V. Mazumder, Ö. Metin and S. Sun, *ACS Catal.*, 2012, **2**, 1290–1295.; (b) Ö. Metin, A. Mendoza-Garcia, D. Dalmizrak, M. S. Gültekin and S. Sun, *Catal. Sci. Technol.*, 2016, **6**, 6137–6143.; (c) Z. Wang, H. Zhang, L. Chen, S. Miao, S. Wu, X. Hao, W. Zhang and M. Jia, *J. Phys. Chem. C*, 2018, **122**, 12975–12983.; (d) T. Karaca, M. Sevim and Ö. Metin, *ChemCatChem*, 2017, **9**, 4185–4190.; (e) F. Fu, C. Wang, Q. Wang, A. M. Martinez-Villacorta, A. Escobar, H. Chong, X. Wang, S. Moya, L. Salmon, E. Fouquet, J. Ruiz and D. Astruc, *J. Am. Chem. Soc.*, 2018, **140**, 10034–10042.; (f) Q. Wang, F. Fu, S. Yang, M. Martinez Moro, M. D. L. A. Ramirez, S. Moya, L. Salmon, J. Ruiz and D. Astruc, *ACS Catal.*, 2019, **9**, 1110–1119.

98 (a) K. Feng, J. Zhong, B. Zhao, H. Zhang, L. Xu, X. Sun and S. T. Lee, *Angew. Chemie - Int. Ed.*, 2016, **55**, 11950–11954.; (b) C. Yu, J. Fu, M. Muzzio, T. Shen, D. Su, J. Zhu and S. Sun, *Chem. Mater.*, 2017, **29**, 1413–1418; (c) Q. Yao, Z. H. Lu, Y. Wang, X. Chen and G. Feng, *J. Phys. Chem. C*, 2015, **119**, 14167–14174.

99 (a) L.-L. Long, X.-Y. Liu, J.-J. Chen, J. Jiang, C. Qian, G.-X. Huang, Q. Rong, X. Zhang and H.-Q. Yu, *ACS Appl. Nano Mater.*, 2018, **1**, 6800–6807.; (b) C. Y. Peng, L. Kang, S. Cao, Y. Chen, Z. S. Lin and W. F. Fu, *Angew. Chemie - Int. Ed.*, 2015, **54**, 15725–15729.

100 (a) M. Navlani-García, K. Mori, D. Salinas-Torres, Y. Kuwahara and H. Yamashita, *Front. Mater.*, **6**.; (b) A. K. Singh, S. Singh and A. Kumar, *Catal. Sci. Technol.*, 2016, **6**, 12–40.

101 (a) S. Zhang, Ö. Metin, D. Su and S. Sun, *Angew. Chemie - Int. Ed.*, 2013, **52**, 3681–3684.; (b) O. Metin, X. Sun and S. Sun, *Nanoscale*, 2013, **5**, 910–912.; (c) X. Gu, Z. H. Lu, H. L. Jiang, T. Akita and Q. Xu, *J. Am. Chem. Soc.*, 2011, **133**, 11822–11825.

102 K. Mori, T. Sano, H. Kobayashi and H. Yamashita, *J. Am. Chem. Soc.*, 2018, **140**, 8902–8909.

103 (a) M. Ojeda and E. Iglesia, *Angew. Chemie - Int. Ed.*, 2009, **48**, 4800–4803.; (b) Q. Y. Bi, X. L. Du, Y. M. Liu, Y. Cao, H. Y. He and K. N. Fan, *J. Am. Chem. Soc.*, 2012, **134**, 8926–8933.

104 (a) C. Yu, X. Guo, Z. Xi, M. Muzzio, Z. Yin, B. Shen, J. Li, C. T. Seto and S. Sun, *J. Am. Chem. Soc.*, 2017, **139**, 5712–5715.; (b) S. J. Li, Y. T. Zhou, X. Kang, D. X. Liu, L. Gu, Q. H. Zhang, J. M. Yan and Q. Jiang, *Adv. Mater.*, 2019, **31.**; (c) J. M. Yan, S. J. Li, S. S. Yi, B. R. Wulan, W. T. Zheng and Q. Jiang, *Adv. Mater.*, 2018, **30**.; (d) Q. Y. Bi, J. D. Lin, Y. M. Liu, H. Y. He, F. Q. Huang and Y. Cao, *Angew. Chemie - Int. Ed.*, 2016, **55**, 11849–11853.

105 (a) Z. Zheng, T. Tachikawa and T. Majima, *J. Am. Chem. Soc.*, 2015, **137**, 948–957.; (b) M. Wen, K. Mori, Y. Kuwahara and H. Yamashita, *ACS Energy Lett.*, 2017, **2**, 1–7.; (c) K. Tedsree, T. Li, S. Jones, C. W. A. Chan, K. M. K. Yu, P. A. J. Bagot, E. A. Marquis, G. D. W. Smith and S. C. E. Tsang, *Nat. Nanotechnol.*, 2011, **6**, 302–307.

106 M. J. Climent, A. Corma, S. Iborra and M. J. Sabater, *ACS Catal.*, 2014, **4**, 870–891.

107 (a) P. Zhang, C. Shao, Z. Zhang, M. Zhang, J. Mu, Z. Guo and Y. Liu, *Nanoscale*, 2011, **3**, 3357–3363.; (b) L. Liu, Y. Liu, Y. Ai, J. Li, J. Zhou, Z. Fan, H. Bao, R. Jiang, Z. Hu, J. Wang, K. Jing, Y. Wang, Q. Liang and H. Sun, *iScience*, 2018, **8**, 61–73.; (c) K. Murugesan, A. S. Alshammari, M. Sohail, M. Beller and R. V. Jagadeesh, *J. Catal.*, 2019, **370**, 372–377.

108 (a) M. Shen, H. Liu, C. Yu, Z. Yin, M. Muzzio, J. Li, Z. Xi, Y. Yu and S. Sun, *J. Am. Chem. Soc.*, 2018, **140**, 16460–16462.

109 (a) H. J. Cho, D. Kim, J. Li, D. Su and B. Xu, *J. Am. Chem. Soc.*, 2018, **140**, 13514–13520.; (b) S. Montolio, C. Vicent, V. Aseyev, I. Alfonso, M. I. Burguete, H. Tenhu, E. García-Verdugo and S. V. Luis, *ACS Catal.*, 2016, **6**, 7230–7237.
110 T. P. Bigioni, X. M. Lin, T. T. Nguyen, E. I. Corwin, T. A. Witten and H. M. Jaeger, *Nat. Mater.*, 2006, **5**, 265–270.
111 C. Yu, X. Guo, M. Muzzio, C. T. Seto and S. Sun, *ChemPhysChem*, 2019, **20**, 23–30.
112 (a) G. Zheng, L. Polavarapu, L. M. Liz-Marzán, I. Pastoriza-Santos and J. Pérez-Juste, *Chem. Commun.*, 2015, **51**, 4572–4575.; (b) E. Hariprasad and T. P. Radhakrishnan, *ACS Catal.*, 2012, **2**, 1179–1186.
113 (a) P. S. Shuttleworth, M. De Bruyn, H. L. Parker, A. J. Hunt, V. L. Budarin, A. S. Matharu and J. H. Clark, *Green Chem.*, 2014, **16**, 573–584.; (b) P. Sudarsanam, E. Peeters, E. V. Makshina, V. I. Parvulescu and B. F. Sels, *Chem. Soc. Rev.*, 2019, 2366–2421.
114 (a) P. Gallezot, *Chem. Soc. Rev*., 2012, **41**, 1538–1558.; (b) F. Jin and H. Enomoto, *Energy Environ. Sci*., 2011, **4**, 382–397.; (c) B. Girisuta, L. P. B. M. Janssen and H. J. Heeres, *Ind. Eng. Chem. Res*., 2007, **46**, 1696–1708.
115 (a) A. S. Piskun, J. Ftouni, Z. Tang, B. M. Weckhuysen, P. C. A. Bruijnincx and H. J. Heeres, *Appl. Catal. A Gen.*, 2018, **549**, 197–206. (b) W. Luo, M. Sankar, A. M. Beale, Q. He, C. J. Kiely, P. C. A. Bruijnincx and B. M. Weckhuysen, *Nat. Commun.*, 2015, **6**, 6540. (c) S. Li, Y. Wang, Y. Yang, B. Chen, J. Tai, H. Liu and B. Han, *Green Chem.*, 2019, **21**, 770–774.
116 (a) J. D. Vidal, M. J. Climent, P. Concepcion, A. Corma, S. Iborra and M. J. Sabater, *ACS Catal.,* 2015, **5**, 5812–5821; (b) J. D. Vidal, M. J. Climent, A. Corma, D. P. Concepcion, and S. Iborra, *ChemSusChem,* 2017, **10**, 119–128.; (c) J. Zhang, B. Xie, L. Wang, X. Yi, C. Wang, G. Wang, Z. Dai, A. Zheng and F. S. Xiao, ChemCatChem, 2017, 9, 2661–2667.
117 C. Xie, J. Song, H. Wu, Y. Hu, H. Liu, Z. Zhang, P. Zhang, B. Chen and B. Han, *J. Am. Chem. Soc.*, 2019, **141**, 4002–4009.
118 (a) L. L. Chng, N. Erathodiyil and J. Y. Ying, *Acc. Chem. Res.*, 2013, **46**, 1825–1837.; (b) A. Corma and H. Garcia, *Chem. Soc. Rev.*, 2008, **37**, 2096– 2126.; (c) C. J. Wrasman, A. Boubnov, A. R. Riscoe, A. S. Hoffman, S. R. Bare and M. Cargnello, *J. Am. Chem. Soc.*, 2018, **140**, 12930–12939. (d) Y. Wang, Z. Chen, R. Shen, X. Cao, Y. Chen, C. Chen, D. Wang, Q. Peng and Y. Li, *Nano Res.*, 2016, **9**, 1209–1219.
119 (a) J. Park, E. Kang, S. U. Son, H. M. Park, M. K. Lee, J. Kim, K. W. Kim, H. J. Noh, J. H. Park, C. J. Bae, J. G. Park and T. Hyeon, *Adv. Mater.*, 2005, **17**, 429–434.; (b) S. U. Son, Y. Jang, J. Park, H. Bin Na, H. M. Park, H. J. Yun, J. Lee and T. Hyeon, *J. Am. Chem. Soc.*, 2004, **126**, 5026–5027.; (c) Ö. Metin, S. F. Ho, C. Alp, H. Can, M. N. Mankin, M. S. Gültekin, M. Chi and S. Sun, *Nano Res.*, 2013, **6**, 10–18.; (d) S. Y. Fu, Y. Z. Li, W. Chu, C. Li and D. G. Tong, *Catal. Sci. Technol.*, 2015, **5**, 1638–1649.
120 (a) H. M. E. Azzazy and M. M. H. Mansour, *Clin. Chim. Acta*, 2009, **403**, 1–8.; (b) Z. Shen, M. P. Nieh and Y. Li, *Polymers*, 2016, **8**, 83.
121 S. M. Moghimi, A. C. Hunter and J. C. Murray, *FASEB J.*, 2005, **19**, 311–330.
122 (a) M. L. Etheridge, S. A. Campbell, A. G. Erdman, C. L. Haynes, S. M. Wolf and J. McCullough, *Nanomedicine Nanotechnology, Biol. Med.*, 2013, **9**, 1–14.; (b) D. Groneberg, M. Giersig, T. Welte and U. Pison, *Curr. Drug Targets*, 2006, **7**, 643–648.
123 N. V. S. Vallabani and S. Singh, *3 Biotech*, 2018, **8**,279.
124 C. Xu and S. Sun, *Dalt. Trans.*, 2009, 5583–5591.
125 (a) H. Wei, N. Insin, J. Lee, H. S. Han, J. M. Cordero, W. Liu and M. G. Bawendi, *Nano Lett.*, 2012, **12**, 22–25.; (b) E. Amstad, M. Textor and E. Reimhult, *Nanoscale*, 2011, **3**, 2819–2843.
126 J. Xie, C. Xu, N. Kohler, Y. Hou and S. Sun, *Adv. Mater.*, 2007, **19**, 3163–3166.
127 J. Xie, C. Xu, Z. Xu, Y. Hou, K. L. Young, S. X. Wang, N. Pourmond and S. Sun, *Chem. Mater.*, 2006, **18**, 5401–5403.
128 (a) J. Xie, K. Chen, J. Huang, S. Lee, J. Wang, J. Gao, X. Li and X. Chen, *Biomaterials*, 2010, **31**, 3016–3022.; (b) J. Xie, J. Wang, G. Niu, J. Huang, K. Chen, X. Li and X. Chen, *Chem. Commun.*, 2010, **46**, 433–435.
129 T. A. Cowger, Y. Yang, D. E. Rink, T. Todd, H. Chen, Y. Shen, Y. Yan and J. Xie, *Bioconjug. Chem.*, 2017, **28**, 890–896.
130 J. Huang, L. Bu, J. Xie, K. Chen, Z. Cheng, X. Li and X. Chen, *ACS Nano*, 2010, **4**, 7151–7160.
131 (a) T. Cowger and J. Xie, *Methods Mol. Biol.*, 2013, **1025**, 225–235.; (b) H.-Y. Lee, Z. Li, K. Chen, A. R. Hsu, C. Xu, J. Xie, S. Sun and X. Chen, *J. Nucl. Med.*, 2008, **49**, 1371–1379.
132 C. C. Berry and A. S. G. Curtis, *J. Phys. D. Appl. Phys.*, 2003, R198–R206.
133 J. V. Jokerst, T. Lobovkina, R. N. Zare and S. S. Gambhir, *Nanomedicine*, 2011, **6**, 715–728.
134 T. A. Cowger, W. Tang, Z. Zhen, K. Hu, D. E. Rink, T. J. Todd, G. D. Wang, W. Zhang, H. Chen and J. Xie, *Theranostics*, 2015, **5**, 1225–1232.
135 J. Huang, L. Wang, R. Lin, A. Y. Wang, L. Yang, M. Kuang, W. Qian and H. Mao, *ACS Appl. Mater. Interfaces*, 2013, **5**, 4632–4639.
136 Y. Matsumura and H. Maeda, *Cancer Res.*, 1986, **46**, 6387–6392.
137 S. K. Golombek, J. N. May, B. Theek, L. Appold, N. Drude, F. Kiessling and T. Lammers, *Adv. Drug Deliv. Rev.*, 2018, **130**, 17–38.
138 W. Tang, Z. Zhen, C. Yang, L. Wang, T. Cowger, H. Chen, T. Todd, K. Hekmatyar, Q. Zhao, Y. Hou and J. Xie, *Small*, 2014, **10**, 1245–1249.
139 (a) Jay S. Desgrosellier and D. A. Cherech, *Nat. Rev. Canver*, 2015, **10**, 9–22.; (b) M. V. Backer and J. M. Backer, *Theranostics*, 2012, **2**, 502-515.
140 J. Xie, K. Chen, H. Y. Lee, C. Xu, A. R. Hsu, S. Peng, X. Chen and S. Sun, *J. Am. Chem. Soc.*, 2008, **130**, 7542–7543.
141 D. N. Ho, N. Kohler, A. Sigdel, R. Kalluri, J. R. Morgan, C. Xu and S. Sun, *Theranostics*, 2012, **2**, 66–75.
142 Q. Quan, J. Xie, H. Gao, M. Yang, F. Zhang, G. Liu, X. Lin, A. Wang, H. S. Eden, S. Lee, G. Zhang and X. Chen, *Mol. Pharm.*, 2011, **8**, 1669–1676.
143 K. Cheng, S. Peng, C. Xu and S. Sun, *J. Am. Chem. Soc.*, 2009, **131**, 10637–10644.
144 C. Xu, J. Xie, D. Ho, C. Wang, N. Kohler, E. G. Walsh, J. R. Morgan, Y. E. Chin and S. Sun, *Angew. Chemie - Int. Ed.*, 2008, **47**, 173–176.
145 C. Xu, B. Wang and S. Sun, *J. Am. Chem. Soc.*, 2009, **131**, 4216–4217.
146 T. Todd, Z. Zhen, W. Tang, H. Chen, G. Wang, Y. J. Chuang, K. Deaton, Z. Pan and J. Xie, *Nanoscale*, 2014, **6**, 2073–2076.

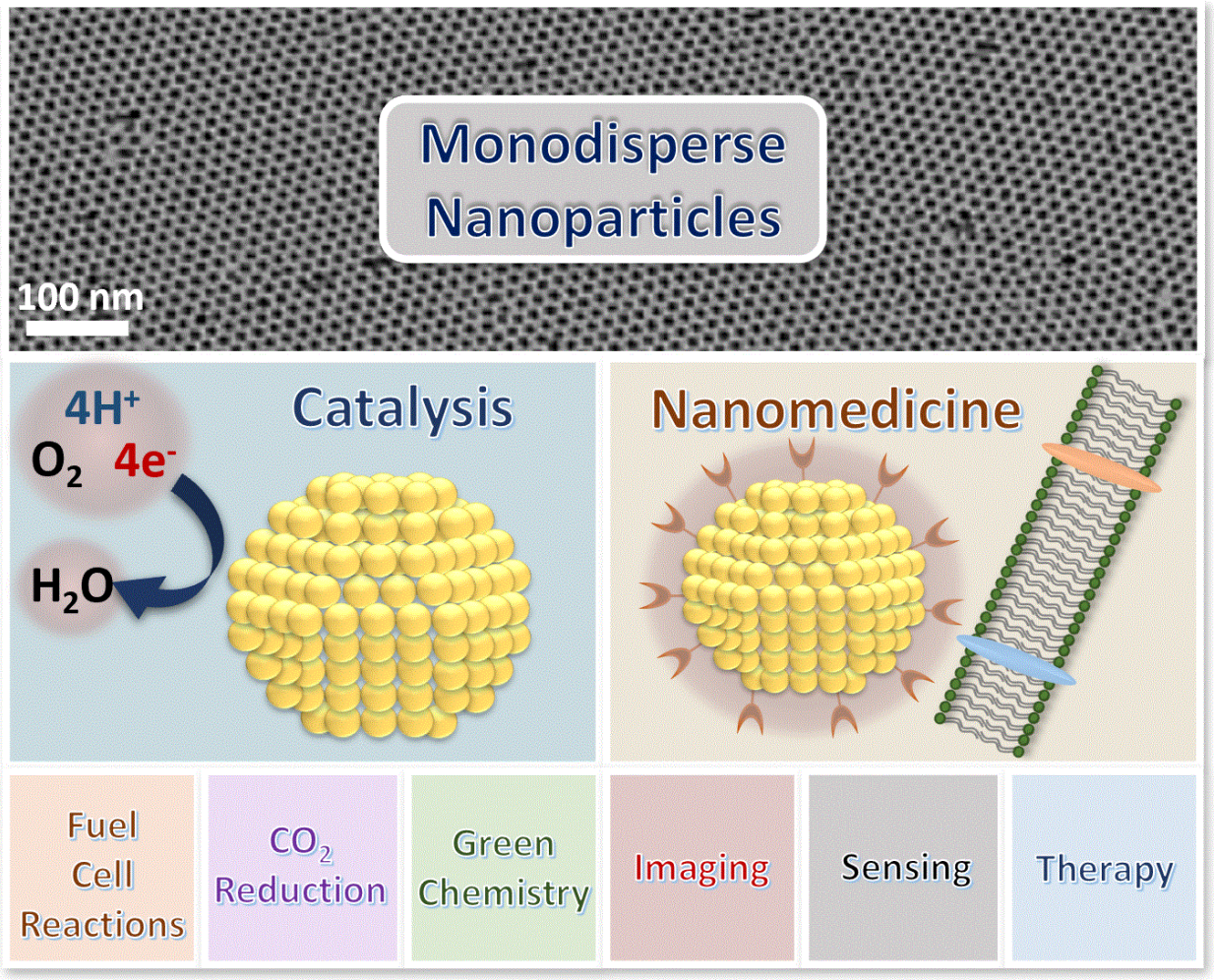

One sentence of text, maximum 20 words:

Monodisperse nanoparticles are successful model systems for understanding structure-property relationships at the nanoscale and applications like catalysis and nanomedicine.